OPEN ACCESS



A Census of Protostellar Outflows in Nearby Molecular Clouds

Duo Xu^{1,2}, Stella S. R. Offner¹, Robert Gutermuth³, Shuo Kong^{4,5}, and Hector G. Arce⁵ Department of Astronomy, The University of Texas at Austin, Austin, TX 78712, USA; soffner@astro.as.utexas.edu

Department of Astronomy, University of Virginia, Charlottesville, VA 22904-4235, USA; xuduo117@utexas.edu

Department of Astronomy, University of Massachusetts, Amherst, MA 01003, USA

Steward Observatory, University of Arizona, Tucson, AZ 85719, USA

Department of Astronomy, Yale University, New Haven, CT 06511, USA

Received 2021 July 25; revised 2021 November 1; accepted 2021 November 13; published 2022 February 8

Abstract

We adopt the deep learning method CASI-3D (Convolutional Approach to Structure Identification-3D) to systemically identify protostellar outflows in 12 CO and 13 CO observations of the nearby molecular clouds, Ophiuchus, Taurus, Perseus, and Orion. The total outflow masses are $267\,M_\odot$, $795\,M_\odot$, $1305\,M_\odot$, and $6332\,M_\odot$ for Ophiuchus, Taurus, Perseus, and Orion, respectively. We show the outflow mass in each cloud is linearly proportional to the total number of young stellar objects. The estimated total 3D deprojected outflow energies are 9×10^{45} erg, 6×10^{46} erg, 1.2×10^{47} erg, and 6×10^{47} erg for Ophiuchus, Taurus, Perseus, and Orion, respectively. The energy associated with outflows is sufficient to offset turbulent dissipation at the current epoch for all four clouds. All clouds also exhibit a break point in the spatial power spectrum of the outflow prediction map, which likely corresponds to the typical outflow mass and energy injection scale.

Unified Astronomy Thesaurus concepts: Interstellar medium (847); Stellar jets (1607); Convolutional neural networks (1938); Young stellar objects (1834); Stellar feedback (1602); Molecular clouds (1072); Star formation (1569); Astronomy data analysis (1858)

1. Introduction

Protostars launch energetic collimated bipolar outflows during the star formation process. This outflow gas entrains and accelerates the surrounding material to higher velocities than that of the ambient cloud gas, injecting a substantial amount of energy into the host molecular cloud (Frank et al. 2014; Bally 2016). Numerical simulations suggest protostellar outflows not only reduce the core and stellar mass (e.g., Hansen et al. 2012; Offner & Chaban 2017) but also depress the star formation rate and star formation efficiency in molecular clouds (e.g., Federrath et al. 2014; Federrath 2015; Cunningham et al. 2018). Meanwhile, protostellar outflows likely control the shape of the stellar initial mass function (IMF; Cunningham et al. 2018; Guszejnov et al. 2021). Theoretical and numerical studies indicate that protostellar outflows are highly efficient at driving turbulent motions (Matzner 2007; Nakamura & Li 2007; Moraghan et al. 2013). In small-to-intermediate-sized clouds, energy injected by protostellar outflows can compensate for rapid turbulent dissipation over at least several dynamical timescales (Cunningham et al. 2006; Li & Nakamura 2006; Matzner 2007; Carroll et al. 2009). Consequently, protostellar outflows may stall the local gravitational collapse of molecular clouds, thereby extending the cloud lifetime (Wang et al. 2010). The role of protostellar feedback on the fate of molecular clouds is still under debate (Bally 2016).

Unfortunately, the mechanism by which protostellar outflows convert their kinetic energy into turbulent energy remains poorly understood observationally (Frank et al. 2014). In practice, astronomers usually evaluate outflow impact by comparing the total kinetic energy from protostellar outflows

Original content from this work may be used under the terms of the Creative Commons Attribution 4.0 licence. Any further distribution of this work must maintain attribution to the author(s) and the title of the work, journal citation and DOI.

with the turbulent energy of their host cloud. For example, Arce et al. (2010) identified 60 outflow candidates in the Perseus molecular cloud and concluded the total outflow energy is sufficient to replenish the dissipation of turbulence. A similar result was also found in Taurus (Li et al. 2015), in Ophiuchus (Nakamura et al. 2011), and in Orion (Feddersen et al. 2020).

Accurately determining the impact of protostellar outflows, especially quantifying their effect on the cloud energy budget, requires a complete census of outflows. However, it is challenging to identify most of the outflows that are deeply embedded in dense clouds (Arce et al. 2010; Dunham et al. 2014a). The morphology of these embedded outflows are not as distinct as isolated ones in low-velocity channels, and the outflowing gas is difficult to separate from the ambient cloud. Protostars are often clustered, and their outflows interact, making visual identification challenging. One solution is to calculate the outflow gas whose velocity is significantly above the cloud velocity dispersion and extrapolate the total mass (Arce et al. 2010; Li et al. 2015; Feddersen et al. 2020). However, this leads to an order-of-magnitude uncertainty (Arce et al. 2010).

Recent developments in machine-learning approaches have enabled automated detection, which can separate outflows from cloud emission and conduct systematic identification of outflow features (Zhang et al. 2020; Xu et al. 2020b). Zhang et al. (2020) employed support vector machines (SVMs) to identify molecular outflows in a dark cloud complex from molecular line emission. Although SVMs perform robustly in classification tasks, they require preprocessing of the raw data cubes, i.e., manually extracting feature vectors that represent the raw data. The choice of input features is determined subjectively by visual inspection, and extracting these features from data cubes is nontrivial. Moreover, the manually extracted features discard part of the information embedded in the raw spectral cubes,

which introduces uncertainty and affects the performance of classification. Convolutional neural networks (CNNs) are a powerful new approach being applied to identify structures or objects in astronomical data, such as exoplanets (Shallue & Vanderburg 2018), stellar feedback bubbles (Van Oort et al. 2019; Xu et al. 2020a), and protostellar outflows (Xu et al. 2020b). Given a labeled training set of images or spectral cube data, CNNs can be applied to efficiently identify features in large surveys. Van Oort et al. (2019) developed a Convolutional Approach to Shell/Structure Identification, CASI, to identify stellar feedback bubbles in 2D density slices and ¹²CO integrated intensity maps. Xu et al. (2020a) and Xu et al. (2020b) successfully extended CASI to CASI-3D, which is able to identify stellar feedback bubbles and protostellar outflows in position-position-velocity (PPV) molecular line spectral cubes. Xu et al. (2020b) applied CASI-3D to ¹²CO observations of the Perseus molecular cloud and identified all 60 previously visually identified outflows. Additionally, CASI-3D found 20 new high-confidence outflows. Apart from structure identification, CASI-3D successfully predicts hidden information in the data cube, such as the fraction of mass associated with feedback, which provides a more accurate feedback mass estimation. Xu et al. (2020a) showed that the actual mass associated with stellar feedback in Taurus is an order of magnitude smaller than the previous visual estimates. These results illustrate the capability of CNNs to identify complex structures and infer embedded information.

In this paper, we adopt the deep learning method CASI-3D to systemically identify protostellar outflows in the nearby molecular clouds, Ophiuchus, Taurus, Perseus, and Orion. We describe CASI-3D and the CO observations of these nearby molecular clouds in Section 2. In Section 3, we present the performance of our CNN models in identifying protostellar outflows in the observational data, calculate the physical properties of outflows, and discuss their impact on the clouds. We discuss the broader impact of outflows and compare them with stellar-wind-driven bubbles in Section 4 and summarize our results and conclusions in Section 5.

2. Data and Method

2.1. COMPLETE Survey

The ^{12}CO J = 1 - 0 (115.271 GHz) and ^{13}CO J = 1 - 0 (110.201 GHz) lines were observed simultaneously in surveys of Ophiuchus, Taurus, and Perseus between 2002 and 2005 using the 13.7 m Five College Radio Astronomy Observatory (FCRAO) Telescope (Ridge et al. 2006; Narayanan et al. 2008). The main beam of the antenna pattern has an FWHM of 45" for ^{12}CO and 47" for ^{13}CO . The data are obtained on the fly, but they are resampled onto a uniform 23" grid (Ridge et al. 2006).

The Ophiuchus data has rms antenna temperatures of 0.98 K and 0.33 K for ^{12}CO and ^{13}CO , respectively. We resampled the spectra with a lower velocity resolution of 0.125 km s $^{-1}$ to ensure a uniform velocity resolution for all regions and to match the resolution of the training set. If the velocity resolution is too low (>0.3 km s $^{-1}$), the structure generated by stellar feedback is not distinguishable across multiple velocity channels. On the other hand, if the velocity resolution is too high (<0.1 km s $^{-1}$), the training data will hit the limitation of GPU memory. The noise levels for the new Ophiuchus ^{12}CO and ^{13}CO spectra are reduced by a factor of

square root of 2–0.69 K and 0.23 K, respectively. The final Ophiuchus data cube has a velocity range between -0.8 and 7.5 km s⁻¹ with 67 channels.

The Taurus data has an rms antenna temperature of 0.28 K for ^{12}CO and 0.125 K for ^{13}CO . There are 80 and 76 channels with 0.26 and 0.27 km s $^{-1}$ spacing for ^{12}CO and ^{13}CO , respectively. The velocity range of the Taurus data spans -5.1 to 14.9 km s $^{-1}$.

−5.1 to 14.9 km s⁻¹.

The Perseus ¹²CO and ¹³CO data have rms antenna temperatures of 0.25 K and 0.2 K, respectively. We resampled the spectra with a lower velocity resolution of 0.125 km s⁻¹ to ensure a uniform velocity resolution for all regions and to match the resolution of the training set. The noise levels for the new ¹²CO and ¹³CO spectra is reduced by a factor of the square root of 2 to 0.17 K and 0.14 K, respectively. The final Perseus data cube has a velocity range between −2.0 and 15.0 km s⁻¹ with 137 channels.

2.2. NRO45 Orion Survey

The ^{12}CO J = 1 - 0 and ^{13}CO J = 1 - 0 observations of Orion A were carried out from 2007 to 2017 by the Nobeyama Radio Observatory 45 m telescope (NRO 45m), using two different receivers (Shimajiri et al. 2015a, 2015b; Ishii et al. 2019; Nakamura et al. 2019). The two maps were calibrated to the same intensity scale and combined on a common grid with a pixel scale of 7."5, which corresponds to an effective angular resolution of 22". Ishii et al. (2019) smoothed the combined map to a velocity resolution of 0.22 km s⁻¹, and further converted the intensity to the main beam temperature scale that is benchmarked with data from FCRAO and the Institute for Radio Astronomy in the Millimeter Range 30 m. The final sensitivity for the 12 CO map is 0.40 K. The velocity range of the Orion data spans -2.9–19.3 km s⁻¹. More detailed descriptions about the data can be found in Kong et al. (2018) and Ishii et al. (2019).

2.3. YSO Catalog

To validate our outflow identifications, we compare our feedback maps with the observed distributions of YSOs. We use the YSO catalog for Ophiuchus and Perseus from the Spitzer Extended Solar Neighborhood Archive (SESNA; R. Gutermuth et al. 2021, in preparation) used by Pokhrel et al. (2020). SESNA uses an updated implementation of the data treatment, source catalog construction, and YSO identification and classification processes on Spitzer surveys (Gutermuth et al. 2009). SESNA classified YSOs into four groups: deeply embedded protostars, Class I YSOs, Class II YSOs, and transition disks. For further analysis, we combine the former two groups as "younger YSOs" and merge the latter two groups as "older YSOs."

We adopt the YSO catalog from Rebull et al. (2010) for Taurus, which contains 215 previously identified YSOs and 148 newly identified YSOs. Rebull et al. (2010) adopted observations from the InfraRed Array Camera (IRAC) and Multiband Imaging Photometer for Spitzer (MIPS) between 2005 and 2007. Rebull et al. (2010) applied color–magnitude criteria to select the YSO candidates and classified these YSO candidates into four different classes: Class I, II, III, and flat. For further analysis, we combine YSOs in Class I and flat into a single category of "younger YSOs" and merge YSOs in Classes II and III into a single category of older YSOs."

We adopt the YSO catalog from Megeath et al. (2012) for Orion, which contains a total of 3479 dusty YSOs from IRAC and MIPS observations. Megeath et al. (2012) classified these YSOs into three categories, which includes 2991 young stars with disks, 428 protostars, and 50 faint candidate protostars. For further analysis, we designate protostars as "younger YSOs" and young stars with disks as "older YSOs."

YSOs in the group of "younger YSOs" have an average age smaller than 1 Myr, while YSOs in the group of "older YSOs" have an average age around 1–3 Myr (Dunham et al. 2014b). However, it is worth noting that truly younger YSOs and older YSOs may be misclassified based on their orientation with respect to the line of sight (LOS; Offner et al. 2012), which means the actual age of an individual YSO in the group of "younger YSOs" is not necessarily younger than that of an object in the group of "older YSOs."

Finally, we note that not all of the surveys completely cover the area of observed molecular emission. We focus our analysis on the areas with YSO coverage and indicate the boundaries of the surveys on the maps.

2.4. Method

2.4.1. CASI-3D

We adopt the previously trained CASI-3D model from Xu et al. (2020b) to identify protostellar outflows in ¹²CO. CASI-3D is an encoder-decoder based CNN combining both residual networks (He et al. 2016) and a "U-net" (Ronneberger et al. 2015). CASI-3D is trained on synthetic ¹²CO data, which models forming stars that launch protostellar outflows. We adopt the same training set and ranges of magnetohydrodynamic (MHD) model properties as described in Xu et al. (2020b, Table 1). We adopt three different ¹²CO abundances and two different cloud kinetic temperatures when conducting synthetic observations as described in Xu et al. (2020b, Table 2). CASI-3D takes ¹²CO data cubes as input and predicts the position of outflows on the voxel level. Xu et al. (2020b) trained two CASI-3D models to identify protostellar outflows. One model, model ME1, is trained to predict the ¹²CO emission that is associated with outflows. The other model, model MF, is trained to predict the fraction of the mass that comes from stellar feedback. A more detailed description of how we generate training data for these two models can be found in Xu et al. (2020b).

2.4.2. Data Preprocessing

Before we apply our CASI-3D models to the observational data, we apply the same preprocessing steps that we adopt for the training data. Due to the relatively large dynamic range of the ¹²CO emission, we take the logarithm of the emission and then normalize the values by subtracting the mean and dividing by the standard deviation of the full map. Figure 1 illustrates the cumulative distribution of normalized emission for the four clouds. Although the ¹²CO emission varies significantly between clouds, after preprocessing, the normalized emission of the four clouds is similar. This allows CASI-3D to perform stably across a variety of conditions.

Xu et al. (2020b) examined the performance of CASI-3D on conditions that are not included in the training set, such as different kinetic temperatures, ¹²CO abundances, beam sizes, and noise levels. CASI-3D is able to successfully identify outflows across a variety of physical and observational

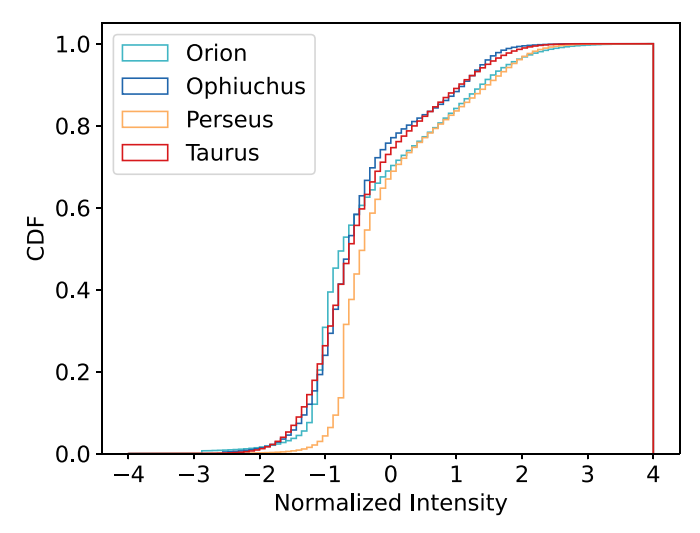


Figure 1. Cumulative distribution function (CDF) of the normalized emission for the four clouds.

conditions. See Appendix C in Xu et al. (2020b) for more details. These tests suggest that the CASI-3D identifications are relatively robust across the range of conditions expected to be characteristic of the observed clouds.

After preprocessing the observational data, we adopt the same strategy as Xu et al. (2020a) to carry out the full ^{12}CO map prediction. We crop the full ^{12}CO map into a stack of 3D chunks. Each chunk has a size of $64 \times 64 \times 32$ (PPV). To reduce the bias due to the position of outflows, each chunk has at least an 84% volume overlap with adjacent chunks. To construct the full-map prediction, we combine the predictions for the individual chunks and adopt the maximum predicted value for each voxel.

2.4.3. Mass Calculations

We follow the same strategy as Arce et al. (2010) to calculate the outflow mass by combining both ¹²CO and ¹³CO data. If there is distinct ¹³CO emission at the corresponding position, we use ¹³CO to calculate the outflow mass. We assume the ¹³CO emission line is optically thin and the ¹²CO emission line is optically thick. We adopt an excitation temperature of 25 K or the ¹²CO peak temperature, whichever is higher, to calculate the mass (Arce et al. 2010; Narayanan et al. 2012; Li et al. 2015; Feddersen et al. 2020). If there is no distinct ¹³CO emission at the corresponding position, we assume the ¹²CO emission line is optically thin to derive the mass. Under the assumption of local thermodynamic equilibrium, the mass estimation scales linearly with the excitation temperature. From previous feedback mass estimates, the choice of excitation temperature ranges from 10 K to 50 K. This could potentially introduce a factor-of-two uncertainty in the mass estimation. We take 62 as the abundance ratio between ^{12}CO and ^{13}CO and 10^{-4} as the abundance ratio between 12 CO and H_2 (Arce et al. 2010; Feddersen et al. 2020). We verify that the ¹³CO emission is generally optically thin for all four clouds. For example, Orion has the largest cloud mass and highest column density among the four clouds. The optical depth of ¹³CO in Orion is less than 1 for 99.4% of the pixels (see also Kong et al. 2018). Only 0.6% of the pixels have $\tau_{13} > 1$, and these are mostly in the OMC-2/3 and L1641-N regions. The maximum value of τ_{13} is 7.8.

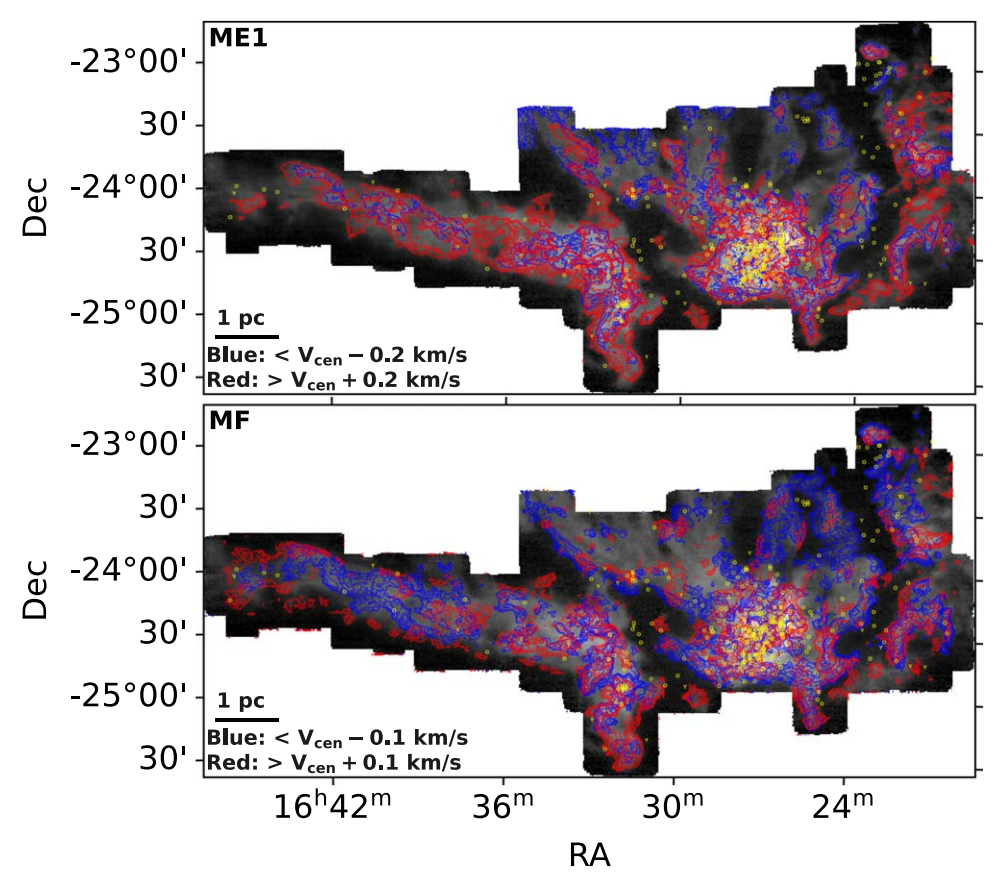


Figure 2. Intensity of 12 CO (1–0) integrated over all velocity channels for Ophiuchus, overlaid with the model ME1 prediction (upper panel in red and blue contours) and with the model MF prediction (lower panel in red and blue contours). Red contours indicate the integrated prediction over the channels that have velocities greater than $V_{\rm cen}+0.4~{\rm km~s^{-1}}$ for model ME1 and $V_{\rm cen}+0.2~{\rm km~s^{-1}}$ for model MF. Blue contours indicate the integrated prediction over the channels that have velocities smaller than $V_{\rm cen}-0.4~{\rm km~s^{-1}}$ for model ME1 and $V_{\rm cen}-0.2~{\rm km~s^{-1}}$ for model MF. "Y" and "O" indicate the location of YSOs, as described in Section 2.3. The contours start at 25th percentile of the sorted pixel values and end at 99.7th percentile of the sorted pixel values of the data, with six levels evenly spaced. It is worth noting that the absolute values of the contour levels for models ME1 and MF are different. The contour levels for the model ME1 prediction start at 2.8 K km s⁻¹ for the blueshifted lobes, and 2.2 K km s⁻¹ for the redshifted lobes, and end at 19.3 K km s⁻¹ and 15.3 K km s⁻¹ for the blue- and redshifted lobes, respectively. The contour levels for the model MF prediction start at 0.80 K km s⁻¹ (blue) and 0.96 K km s⁻¹ (red), and end at 7.2 K km s⁻¹ (blue) and 8.6 K km s⁻¹ (red). The method of plotting contours is the same for Figures 4, 5, 7, and 8.

3. Results

3.1. Outflows Identified in the Full Map

In this section, we present the prediction by models ME1 and MF on the four star-forming clouds (Ophiuchus, Taurus, Perseus, and Orion). Most molecular clouds have a global velocity gradient, which indicates there is no one unique central velocity of a cloud. To better visualize the blueshifted and redshifted lobes of outflows, we remove the large-scale gradient to make local outflow motions clearer, i.e., shifting the velocity zero-point to the flux-weighted central velocity of the spectrum for each pixel. We calculate the flux-weighted central velocity from the first moment maps. In order to reduce the velocity fluctuations on small scales, we apply a Gaussian kernel with an FWHM that corresponds to 0.1 pc to convolve the first moment maps. For each pixel, we show the integrated prediction over the channels that have absolute velocities greater than the central velocity by the specified thresholds.

3.1.1. Ophiuchus

Figure 2 shows ME1 and MF model predictions for Ophiuchus. Both models identify a large amount of outflow

activity in the region of the large, central star cluster. In contrast, the models identify much less outflow activity just north of the cluster, which has only a few YSOs.

Figure 3 shows the predicted outflow activity by models ME1 and MF toward the young star cluster region Lynds 1688 in Ophiuchus. The L1688 region has over 120 young stars and a large number of interacting outflows. Model ME1, which performs similarly to human visual identification, identifies almost everything as feedback in this region. In contrast, Model MF provides an approach to disentangle the outflow emission from the ambient cloud emission. Quantitatively, model ME1 predicts 81% of the mass in this region as outflows. However, model MF predicts that only 12% of the total mass is associated with outflows. Figure 3 shows that both models ME1 and MF are able to identify coherent high-velocity structures in the position–velocity diagram.

It is challenging to separate outflow emission from the cloud emission in ¹²CO (1–0) "by eye," since the cloud emission dominates the ¹²CO (1–0) emission. Consequently, even an expert astronomer can only separate the high-velocity component from the host cloud emission but cannot identify the outflow morphology near the rest-frame velocity of the cloud.

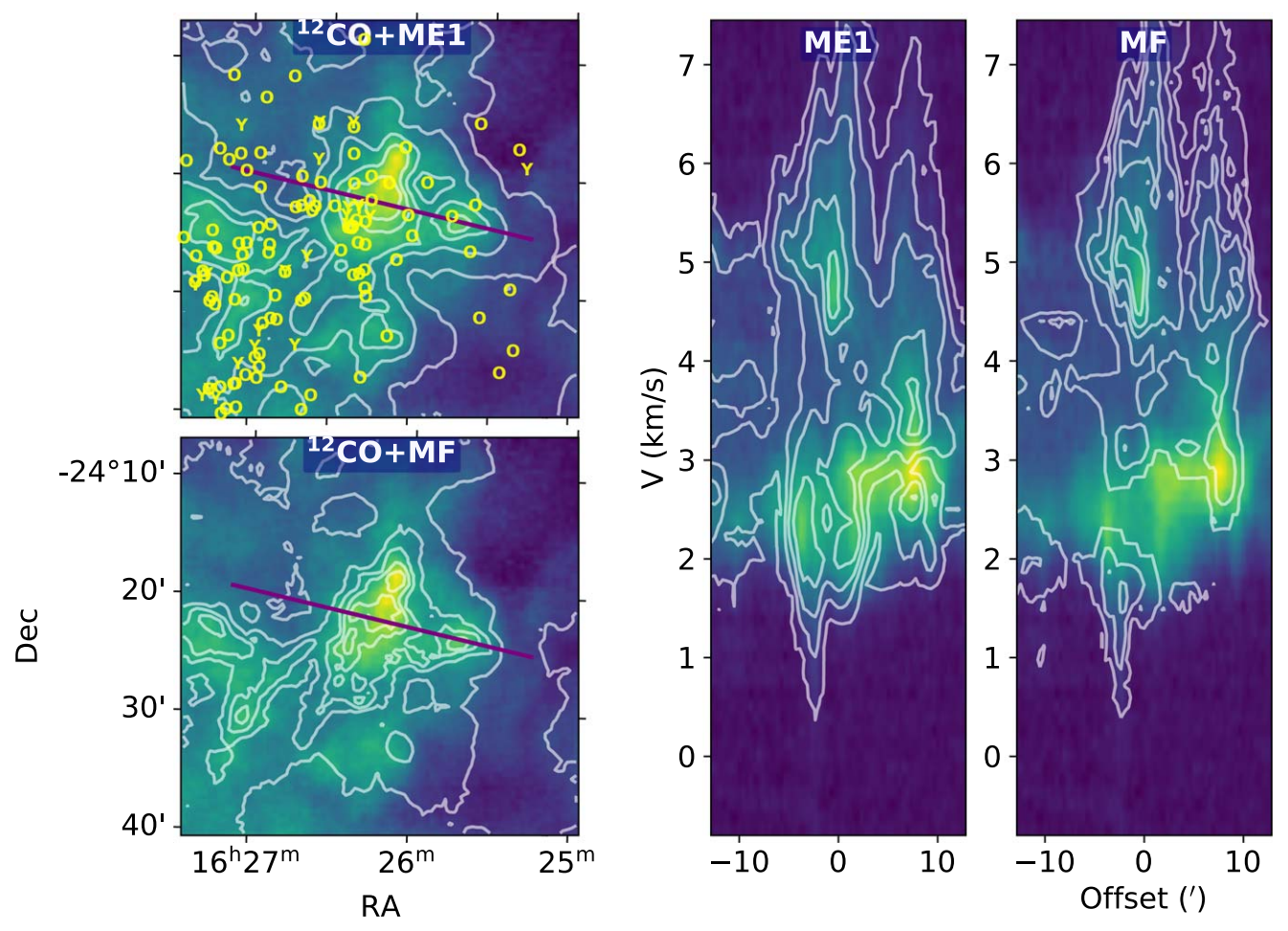


Figure 3. Position–velocity diagram of ¹²CO emission toward the Ophiuchus L1688 region. Left panel: integrated intensity of ¹²CO over the full velocity range (from -0.8 to 7.5 km s⁻¹) overlaid with the model ME1 and MF predictions in white contours. Letters "Y" and "O" mark YSO positions, as described in Section 2.3. The purple line illustrates the cut direction of the position–velocity diagram. Middle and right panel: position–velocity diagram of ¹²CO emission overlaid with the model ME1 and MF predictions in white contours.

3.1.2. Taurus

Figures 4 and 5 show the ME1 and MF model predictions for Taurus. The structures in the outflow prediction maps are more discrete than those in Ophiuchus. One possible reason is that YSOs in Taurus are more sparsely distributed than those in Ophiuchus. Although the total number of YSOs in Taurus is slightly larger, they are less clustered. In Ophiuchus, the outflows driven by YSOs are more likely to interact and overlap with each other. While in Taurus, the outflows are more isolated.

Figure 6 shows the outflow activity predicted by models ME1 and MF toward a previously identified outflow, TMO_06 (Li et al. 2015), in Taurus. Several young YSOs are located around this outflow. Both models are able to identify the blueshifted and redshifted lobes of this outflow. However, the model MF prediction is more extended in the position–velocity diagram. In high-velocity channels, the ¹²CO emission produced by outflows is usually faint while the fraction of outflow mass is high. Model ME1 only identifies the location of outflows and gives stronger emission a higher weight. In this subregion, model ME1 predicts that 43% of the mass in this region is associated with outflows. However, model MF predicts that only 8% of the total mass is outflows gas.

3.1.3. Perseus

Xu et al. (2020b) followed up previous visually identified outflow targets and validated the model performance. Here we extend that analysis by carrying out a "blind search" where we analyze the full cloud. Figure 7 shows the full-map predictions for both models. Both model ME1 and MF predictions are more concentrated toward star clusters. The model ME1 prediction is more spatially extended than that by model MF. This might be caused by a strong emission region with a low outflow mass fraction, where model ME1 counts the entire voxel as feedback while model MF recognizes that much of this emission is cloud contamination and excludes it.

3.1.4. Orion

Figure 8 shows the model ME1 and MF predictions for Orion. Due to the large number of old evolutionary stage YSOs in Orion, we only show the younger YSOs to reduce confusion. We show the position of all Orion YSOs in Figure 22 in Appendix C. The prediction by both models covers most of the emission in Orion, which indicates outflows exist everywhere. This is consistent with the extremely dense distribution of YSOs in Orion.

Figure 9 shows the predicted outflow activity by models ME1 and MF toward a previously identified outflow, Outflow

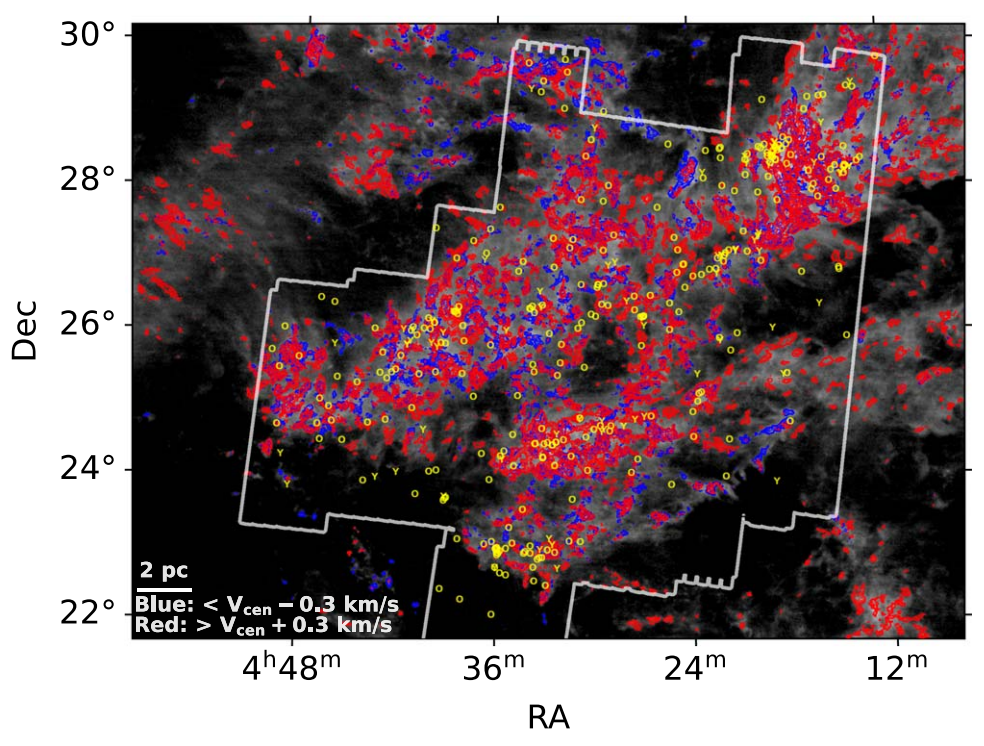


Figure 4. Intensity of ¹²CO (1–0) integrated over all velocity channels for Taurus, overlaid with the model ME1 prediction (red and blue contours). Letters "Y" and "O" mark YSO positions, as described in Section 2.3. The gray line encloses the Spitzer coverage, where YSOs are identified (Rebull et al. 2010). The contours start at the 25th percentile of the sorted pixel values (0.47 K km s⁻¹, for blue contours and 0.49 K km s⁻¹, for red contours) and end at the 99.7th percentile of the sorted pixel values of the data (2.9 K km s⁻¹, for blue contours and 3.4 for red contours), with six levels evenly spaced. Note that the absolute values of the contour levels for models ME1 and MF are different.

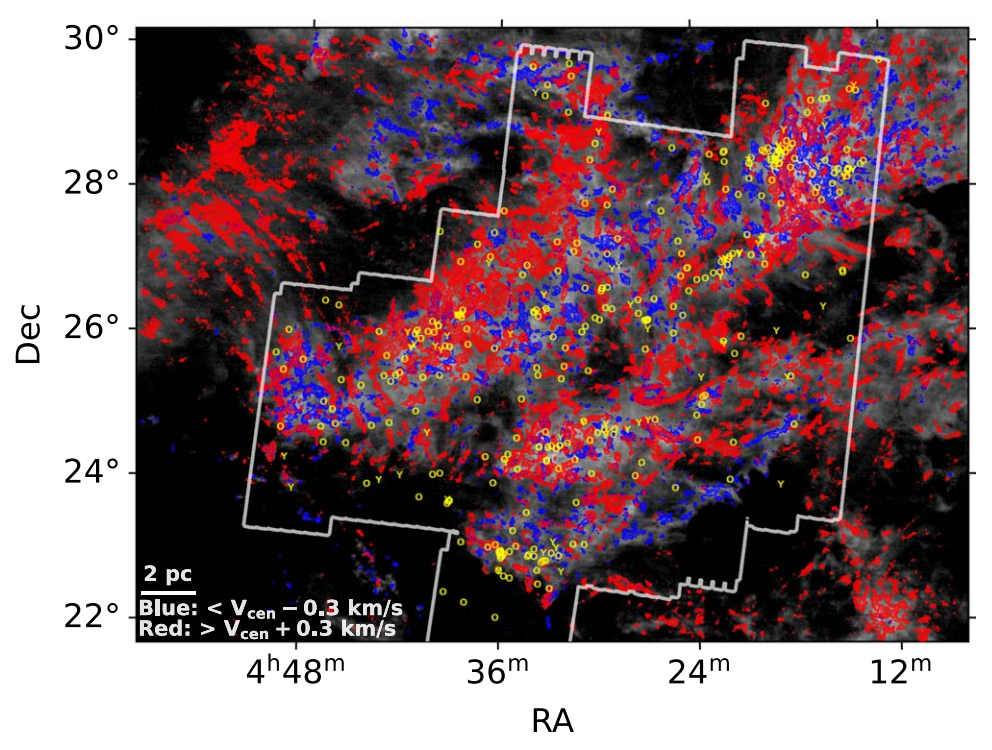


Figure 5. Intensity of 12 CO (1–0) integrated over all velocity channels for Taurus, overlaid with the model MF prediction (red and blue contours). Letters "Y" and "O" mark YSO positions, as described in Section 2.3. The gray line encloses the Spitzer coverage, where YSOs are identified (Rebull et al. 2010). The contours start at the 25th percentile of the sorted pixel values (0.27 K km s⁻¹, for blue contours and 0.27 K km s⁻¹, for red contours) and end at the 99.7th percentile of the sorted pixel values of the data (1.7 K km s⁻¹, for blue contours and 1.5 for red contours), with six levels evenly spaced.

No. 7 (Tanabe et al. 2019), in Orion. Both models similarly highlight the coherent high-velocity structures. There are several young YSOs located around this outflow, which could

be the driving source. For reference, we illustrate the high-velocity components in blue and red contours, which are considered to be outflows by Tanabe et al. (2019). The mass of

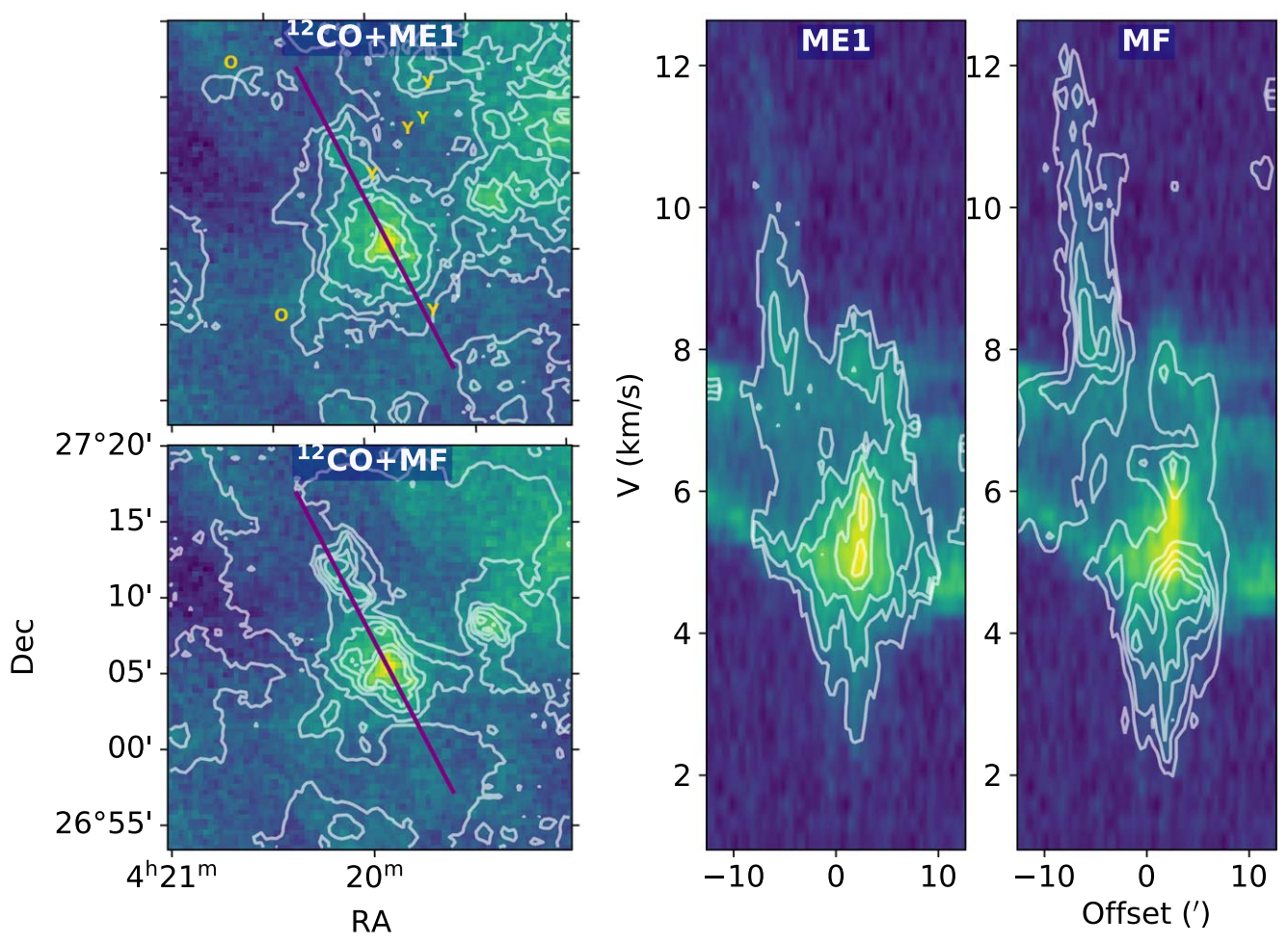


Figure 6. Position–velocity diagram of ¹²CO emission toward a previously identified outflow, TMO_06 (Li et al. 2015), in Taurus. Left panel: integrated intensity of ¹²CO over the full velocity range (from -1.5 to 13.4 km s⁻¹) overlaid with the model ME1 and MF predictions in white contours. Letters "Y" and "O" mark YSO positions, as described in Section 2.3. The purple line illustrates the cut direction of the position–velocity diagram. Middle and right panels: position–velocity diagram of ¹²CO emission overlaid with the model ME1 and MF predictions in white contours.

these high-velocity components is $268 M_{\odot}$. Model MF predicts the outflow mass to be $308 M_{\odot}$, which is similar to previous estimates. In this subregion, model ME1 predicts 61% of the mass in this region is associated with outflows. However, model MF predicts that only 13% of the total mass is outflow gas.

3.2. Physical Properties of Outflows

In this section, we study the physical properties of the outflows we identified and analyze the correlation between the physical quantities of outflows and the number of YSOs in the clouds. This analysis help us evaluate the robustness of the outflow identification by CASI-3D. If the outflows are accurately identified by CASI-3D, we should expect a linear correlation between the outflow mass and the number of YSOs. This is exactly what we find in this Section and Section 3.3. Because our analysis aims to correlate the physical properties of outflows with the number of YSOs, we only calculate mass, energy, and momentum of outflows in the source catalog covered area.

We follow the method in Section 2.4.3 to calculate the mass of outflows. We adopt the model MF estimates for the fiducial values. Figure 10 shows the mass estimates for the outflows in the four molecular clouds. When there are more YSOs in the

region, the predicted outflow mass is higher. In Ophiuchus, on average, each YSO (including both young and old) contributes 0.43 M_{\odot} outflow mass to the host cloud. The values are 1.7 M_{\odot} , 2.8 M_{\odot} , and 3.4 M_{\odot} for Taurus, Perseus, and Orion, respectively. On average, in each of the four clouds, the total mass associated with feedback is about 10% of the mass of the host cloud within the area studied.

We define the 1D LOS momentum as the sum of the gas mass in each channel multiplied by the channel velocity, where we have shifted the mean cloud velocity to zero. To better quantify LOS momentum, we subtract the central velocity along each sightline to reduce the effect of large velocity gradients across the entire cloud, as described in Section 3.1. Subtracting the velocity gradient provides a better estimate of LOS momentum, which reduces the impact of large-scale motions on our estimates. For comparison, we also calculate the LOS moment without subtracting the velocity gradient. The LOS momenta of the outflows and the host clouds are calculated by the following equations

$$P(VGsub) = \sum_{i,j,k} M_{CO,i,j,k}(v_{i,j,k} - \overline{v_{i,j}}),$$
(1)

$$P(VGnonsub) = \sum_{i,j,k} M_{CO,i,j,k}(v_{i,j,k} - \overline{v_{global}}).$$
 (2)

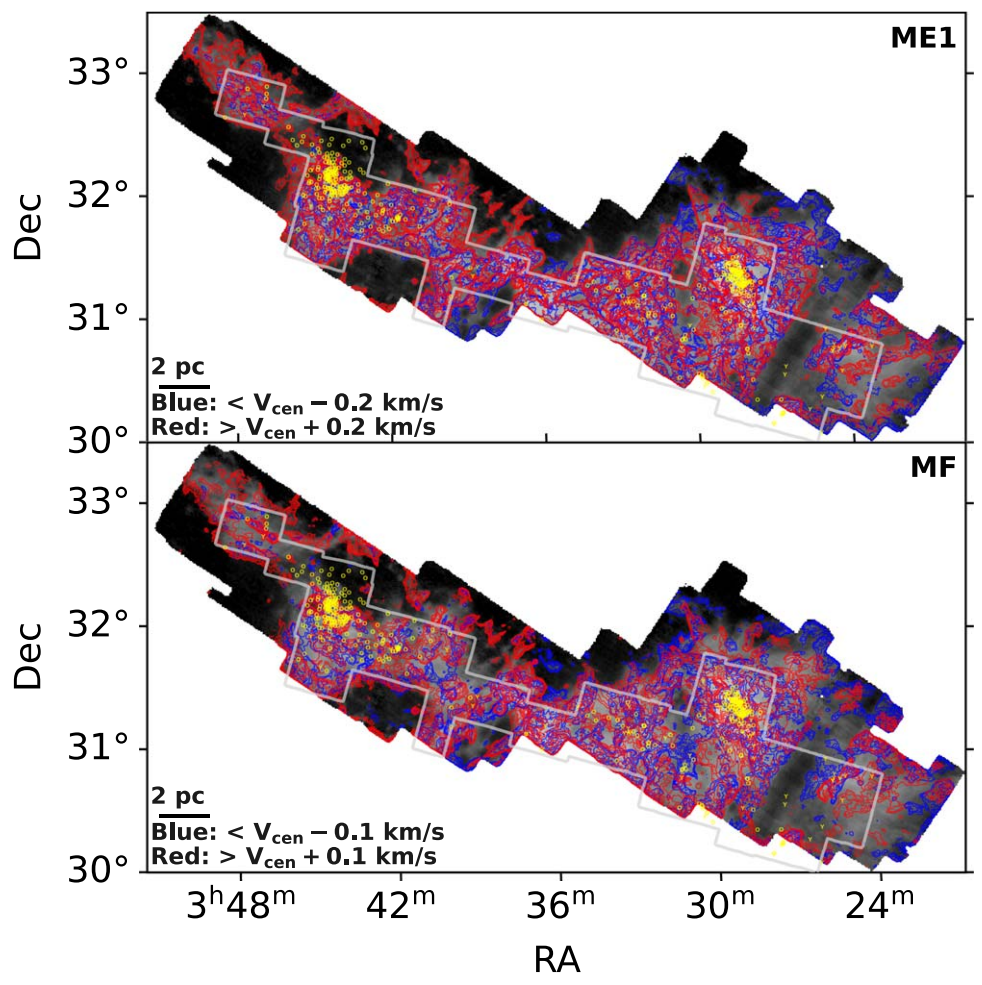


Figure 7. Intensity of 12 CO (1–0) integrated over all velocity channels for Perseus, overlaid with the model ME1 prediction (upper panel in red and blue contours) and with the model MF prediction (lower panel in red and blue contours). Letters "Y" and "O" mark YSO positions, as described in Section 2.3. The gray line encloses the Spitzer coverage, where YSOs are identified (R. Gutermuth et al. 2021, in preparation). The contour levels for the model ME1 prediction start at 2.5 K km s⁻¹ (blue) and 2.1 K km s⁻¹ (red), and end at 17 K km s⁻¹ (blue) and 15 K km s⁻¹ (red). The contour levels for the model MF prediction start at 0.96 K km s⁻¹ (blue) and 0.90 K km s⁻¹ (red), and end at 8.6 K km s⁻¹ (blue) and 8.0 K km s⁻¹ (red).

Similarly, we define the LOS kinetic energy as

$$E\left(VGsub\right) = \sum_{i,j,k} \frac{1}{2} M_{\text{CO},i,j,k} (v_{i,j,k} - \overline{v_{i,j}})^2, \tag{3}$$

$$E\left(VGnonsub\right) = \sum_{i,j,k} \frac{1}{2} M_{CO,i,j,k} (v_{i,j,k} - \overline{v_{global}})^{2}.$$
 (4)

Figure 11 shows the LOS outflow momentum estimates for the four molecular clouds. We list two sets of momentum estimates: one that subtracts the velocity gradient and a second that does not subtract the velocity gradient. We adopt the momentum estimate by model MF, which subtracts the velocity gradients as the fiducial estimate. The trend between the momentum driven by outflows and the number of YSOs is similar to that of the mass estimates for four clouds. In Ophiuchus, the 1D momentum driven by outflows is around 10% of the total 1D momentum of the host cloud. In Taurus, this momentum ratio is 8%. In Perseus and Orion, the 1D momentum driven by outflows is around 16% of the total 1D momentum, which indicates there are likely more high-velocity structures identified as outflows. This is consistent with the star formation history of these clouds. Taurus has a relatively low

star formation rate and mainly forms low-mass stars. On the other hand, Ophiuchus and Orion are home to clusters forming higher-mass stars and have more active star formation. Perseus also contains some intermediate-mass stars, including a couple of B-type stars (Arce et al. 2011).

Ophiuchus, Perseus, and Orion have larger velocity gradients than Taurus, which indicates these clouds contain more complex cloud kinematic structure. These velocity gradients are likely caused by large-scale processes, such as gas accretion (Klessen & Hennebelle 2010) or converging atomic gas flows caused by spiral density waves (Wolfire et al. 1995; Heitsch et al. 2006). Given the magnitude of these bulk motions, we expect that the momentum estimate that includes the velocity gradient overestimates the contribution of outflows, while the momentum that subtracts the velocity gradient provides a better estimate.

Figure 12 shows the LOS outflow kinetic energy for the four molecular clouds. We adopt the kinetic energy estimates by model MF that subtracts the velocity gradient for the comparisons. In Ophiuchus, the LOS kinetic energy injected by outflows is around 6% of the total LOS kinetic energy of the host cloud. In Taurus, this energy ratio is 4%. In Perseus and Orion, the LOS kinetic energy injected by outflows is around 14% of the total LOS kinetic energy. Since kinetic energy is

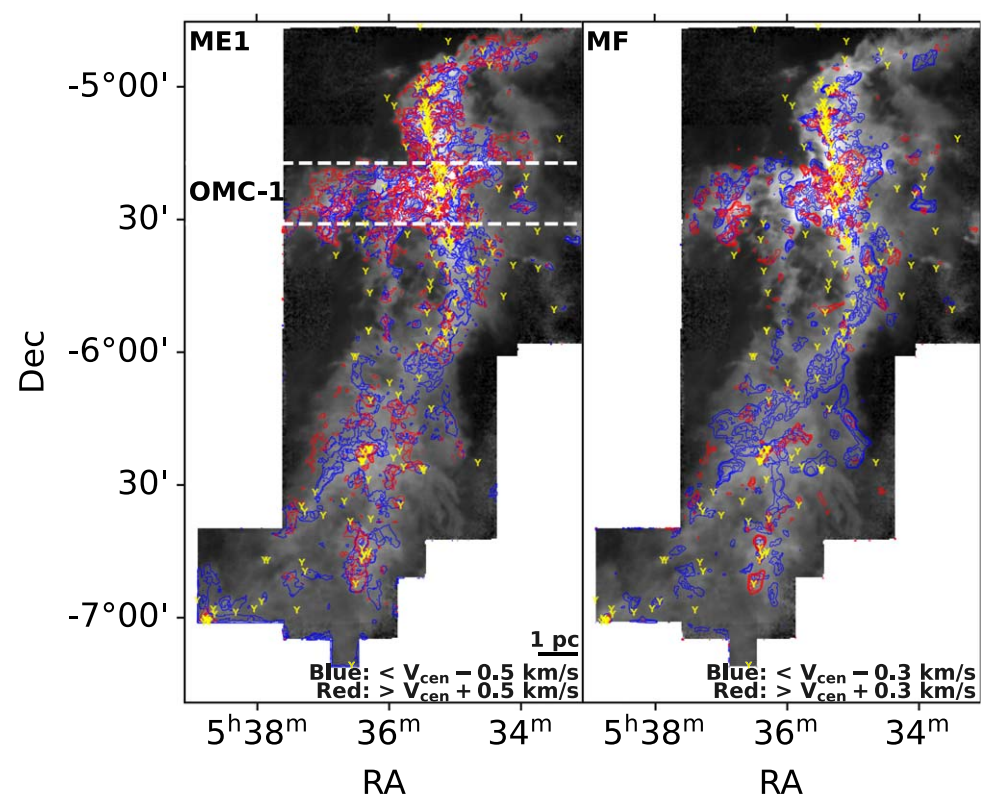


Figure 8. Intensity of ¹²CO integrated over all velocity channels for Orion, overlaid with the model ME1 prediction (left panel in red and blue contours) and with the model MF prediction (right panel in red and blue contours). Letters "Y" mark young YSO positions, as described in Section 2.3. The contour levels for the model ME1 prediction start at 2.1 K km s⁻¹ (blue) and 2.6 K km s⁻¹ (red), and end at 14 K km s⁻¹ (blue) and 18 K km s⁻¹ (red). The contours levels for the model MF prediction start at 0.48 K km s⁻¹ (blue) and 0.55 K km s⁻¹ (red), and end at 4.3 K km s⁻¹ (blue) and 4.9 K km s⁻¹ (red).

proportional to v^2 , one caveat here is that a small amount of mass located at high velocities likely dominates the kinetic energy estimates. However, due to observational limits, some high-velocity gas emission vanishes into background noise, such that our kinetic energy calculation is likely an underestimate. As discussed in Xu et al. (2020b), this could potentially introduce a factor-of-two uncertainty.

3.3. Correlation between the Outflow Properties and the Number of YSOs

In this section, we study the correlation between the total mass, momentum, and energy associated with outflows and the number of YSOs. Due to the extended and overlapping nature of the outflow emission, it is not possible to definitively associate particular sources with particular outflows. Instead, we consider an approach that independently counts the number of YSOs and the outflow impact in a region. We define a "window" to scan through the entire cloud region. We adopt window sizes of 0.5 pc \times 0.5 pc, 1 pc \times 1 pc, and 2 pc \times 2 pc to scan Ophiuchus, and $2 \text{ pc} \times 2 \text{ pc}$, $3 \text{ pc} \times 3 \text{ pc}$, and $5 \text{ pc} \times 5 \text{ pc}$ to scan Taurus and Orion. Since Perseus has the poorest physical resolution, and its full map is narrow, we only adopt window sizes of $2 \text{ pc} \times 2 \text{ pc}$ and $3 \text{ pc} \times 3 \text{ pc}$ to prevent the window exceeding the region. We examine the effect of our choice of window sizes in Appendix A. We set a scanning step size such that each box overlaps with its neighbors by at least 80%. We calculate the mass, momentum, and energy inside the window and count the number of YSOs inside. We consider the outflow relationship between the number of both young YSOs and total YSOs.

Figure 13 shows the correlation between the mass associated with feedback and the number of YSOs in the four clouds. The outflow mass grows linearly with the number of young YSOs for all four clouds. However, the clouds have different offsets, indicating that the outflow mass per young YSO varies. Orion has the most mass associated with outflows per young YSO. However, Orion also has a very large population of older YSOs, which may also drive outflows. The right panel of Figure 13 shows that the correlation between the outflow mass and the number of total YSOs is tighter, and most of the separation between different clouds disappears. There is a linear relation between the outflow mass and the number of all YSOs, where on average, each YSO is associated with 1 M_{\odot} of outflow material. The outflow mass directly launched by the protostar is expected to be 10%-30% of the accreted gas, i.e., 10%-30% of the star mass (e.g., Shu et al. 1988; Pelletier & Pudritz 1992). However, here our outflow estimate also counts entrained mass, which is much higher (e.g., Offner & Chaban 2017). Our results suggest 1 M_{\odot} of outflow material per source. Assuming a 1 M_{\odot} star, for example, theoretical models for outflow launching predict that the outflow mass directly launched would be about 0.1–0.3 M_{\odot} (e.g., Shu et al. 1994; Bontemps et al. 1996). This implies that 0.7–0.9 M_{\odot} of the outflow gas we identify is entrained. This gives a massloading factor of 2.3–9. This is comparable to the mass-loading factor estimated from simulations of individual protostars and the average core-mass-function to stellar IMF offset (Machida & Hosokawa 2013; Offner & Arce 2014; Offner & Chaban 2017). It is worth noting that our outflow estimate is larger than previous observational estimates. The main reason is that CASI-3D is able to capture the outflow material that has

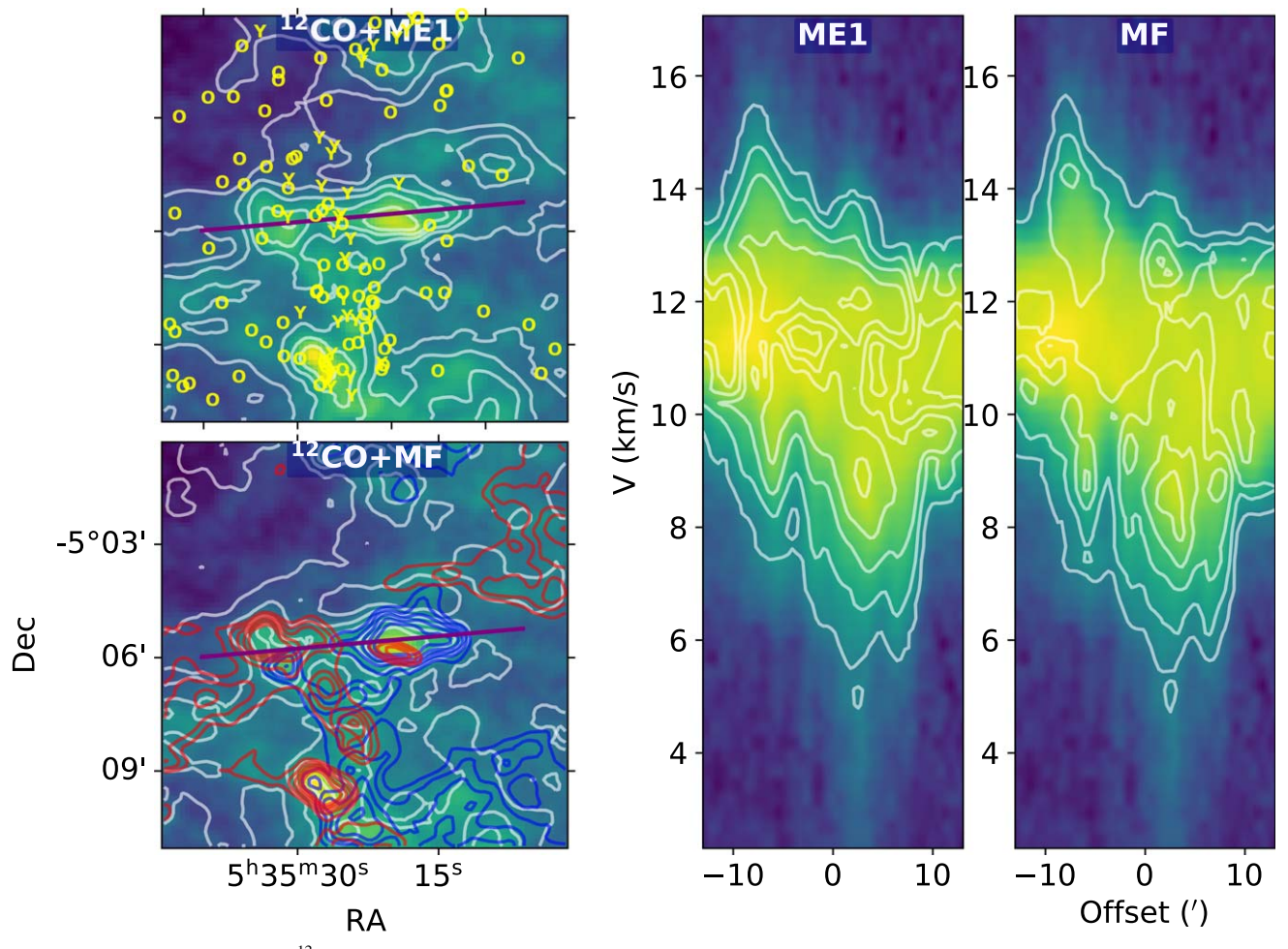


Figure 9. Position–velocity diagram of ¹²CO emission toward a previously identified outflow, Outflow No. 7 (Tanabe et al. 2019), in Orion. Left panel: integrated intensity of ¹²CO over the full velocity range (from 2.3 to 17.1 km s⁻¹) overlaid with the model ME1 and MF predictions in white contours. The blue and red contours indicate the high-velocity components, integrated over the raw emission with velocity ranges of 2.3–9.5 km s⁻¹ and 12.3–17.0 km s⁻¹, respectively. Letters "Y" and "O" mark YSO positions, as described in Section 2.3. The purple line illustrates the cut direction of the position–velocity diagram. Middle and right panels: position–velocity diagram of ¹²CO emission overlaid with the model ME1 and MF predictions in white contours.

relatively low velocities. The low-velocity outflowing gas entrains a significant amount of mass that also contributes to the momentum and kinetic energy of the host cloud, but it is not possible to separate this gas from the ambient gas by eye. Previous work mainly considered the high-velocity outflow mass only.

Younger sources power stronger outflows (Bally 2016), so we might expect a tighter relation between the outflow mass and the number of young YSOs. However, we see better correlation between outflow mass and the total YSO number. There are several possible explanations. First, low-mass sources, with ages up to 3-4 Myr (Bally 2016) continue to launch outflows, albeit weaker ones. We discuss an example in Section 4.1, where an outflow is likely driven by old evolutionary stage YSOs. Second, although young YSOs have a higher mass-loss rate, the outflow mass is a combination of both the mass-loss rate and the launching duration. The older YSOs likely have ejected a significant amount of gas by the time they are observed. In addition, our method may include outflow "relics." The dissipation timescale of outflow features produced by young stars is much longer than the lifetime of the driving source. These fossil outflows might remain even as their driving sources evolve to older evolutionary stages. Cunningham et al. (2006) found a similar scenario in numerical simulations, where fossil outflows retain speeds above the

turbulent velocity for a timescale that is 10 times the duration of their driving source. Similarly, Offner & Chaban (2017) found in simulations that although the high accretion and active outflow phase lasts for $\sim\!0.05\,\mathrm{Myr}$, their impact on the velocity dispersion of the host clouds remains for several 0.1 Myr.

In our outflow mass estimate, a significant amount of the total outflow mass is derived from emission in the cloud velocity channels ($|\nu| \lesssim 1~{\rm km\,s^{-1}}$). This raises the concern that our results may be contaminated by dense, non-outflow material. In Appendix E we evaluate the effect of dense gas contamination on the derived outflow masses and YSO relations. We show that our outflow mass estimate is not significantly contaminated by dense gas.

We show the correlation between the outflow momentum and the number of YSOs in Figure 13. The trend is similar to that of outflow mass. On average, one YSO injects $1 M_{\odot} \, \mathrm{km \, s^{-1}}$. This indicates the mass-weighted LOS velocity is $1 \, \mathrm{km \, s^{-1}}$, which is even smaller than the cloud turbulent velocity derived from $^{12}\mathrm{CO}$. This is because the $^{13}\mathrm{CO}$ emitting region dominates the mass of the cloud and the outflows, which usually has a velocity dispersion only half that of $^{12}\mathrm{CO}$. For example, after subtracting the velocity gradients, the $^{12}\mathrm{CO}$ velocity dispersion in Orion is $\sim 1.5 \, \mathrm{km \, s^{-1}}$, while that of $^{13}\mathrm{CO}$ is only $0.8 \, \mathrm{km \, s^{-1}}$. The massweighted LOS velocity dispersion in Orion is $0.98 \, \mathrm{km \, s^{-1}}$. Model

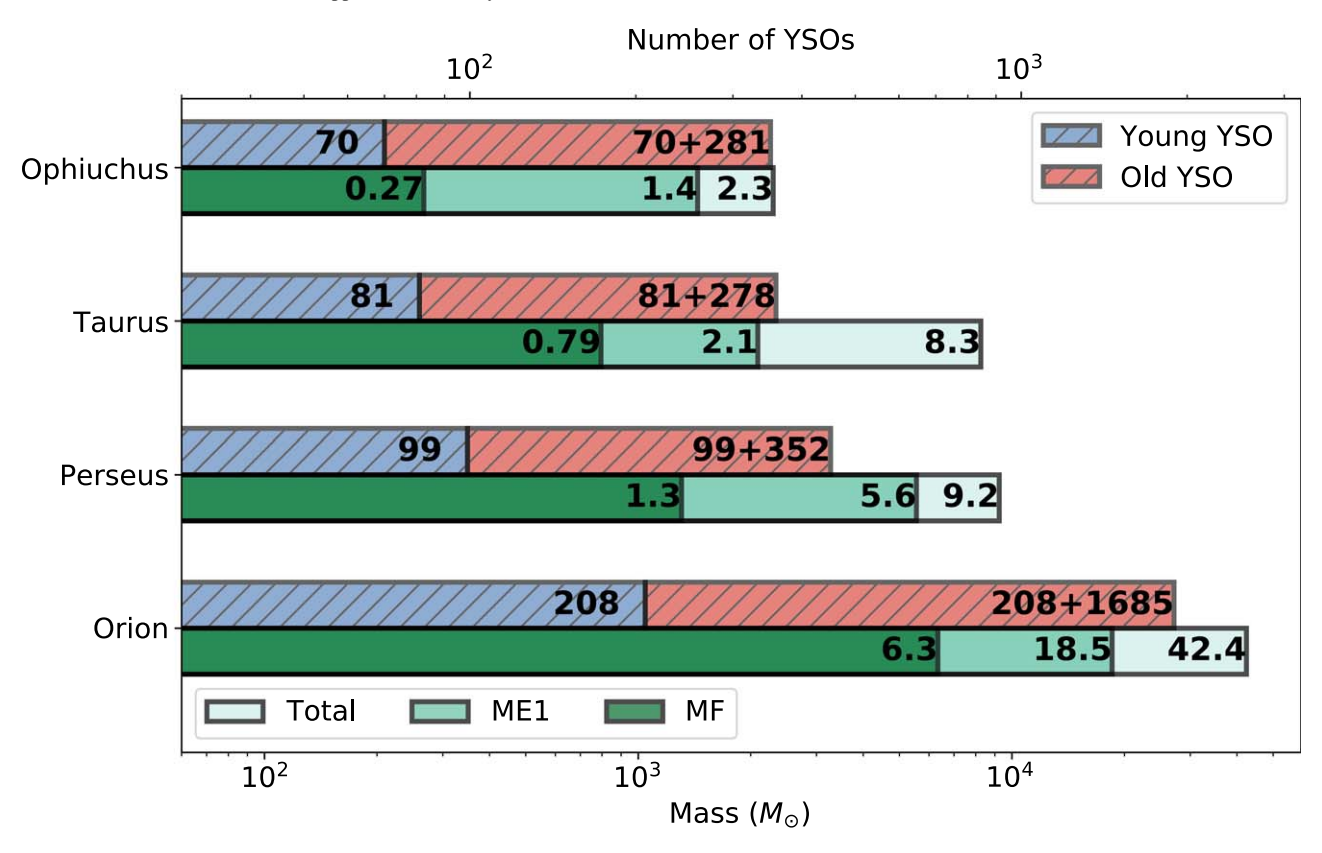


Figure 10. Outflow mass (solid green colors) and the number of YSOs (hatched blue and red) in the four molecular clouds. Numbers in the hatched bars indicate the number of YSOs. Numbers in the unhatched bars indicate the gas mass in units of $10^3 M_{\odot}$. The total mass indicates the mass of the host cloud within the area studied.

MF predicted outflow gas has an LOS velocity dispersion of $1.02~{\rm km~s^{-1}}$ in Orion. All of these numbers are similar for the four clouds. Although the outflow $^{12}{\rm CO}$ emission spans 2–3 km s $^{-1}$ across the velocity channels, most of the mass is associated with gas within 0.8 km s⁻¹ of the cloud mean velocity, i.e., the ¹³CO emitting regions. Near the rest-frame velocity channels, the gas mass increases significantly, but the fraction of gas associated with feedback drops. Consequently, there is a competition between these two effects. Xu et al. (2020b) examined the outflow mass located near the rest-frame velocity, which was ignored in previous outflow surveys. As shown in Figures 16 and 17 in Xu et al. (2020b), the rest-frame gas that is associated with the outflows accounts for almost 75% of the total outflow mass. Thus, the mass-weighted LOS velocity is relatively low, because highvelocity gas contributes only a small portion of the total outflow mass. In addition, the resolution and low signal-to-noise of the data makes detecting high-velocity outflow emission difficult. Consequently, the mass-weighted LOS velocity of outflows is only 1 km s⁻¹ for all four clouds. We show a position-velocity diagram of an outflow in ¹³CO in Appendix D.

Our mass-weighted LOS outflow velocity of 1 km s⁻¹ is low compared to typical outflow velocities estimated in previous works of 1–4 km s⁻¹ (e.g., Arce et al. 2010). This is caused by the mass-weighting. In most cases, observers discard the restframe gas emission, whose outflow morphology is difficult to identify. This leads to a higher LOS velocity estimate. However, CASI-3D is able to pick out the outflow emission from the confused ambient gas emission near the rest-frame velocity. Although the fraction of mass associated with feedback is low, perhaps a few percent, the total mass near rest frame, especially in ¹³CO emission channels, is

significantly higher than that located at high-velocity channels. After correcting for the contamination, the outflow gas near the rest frame still dominates the total mass, which is consistent with the conclusion in Xu et al. (2020b). On the other hand, high-velocity gas is less dense and may be lost in the background noise. Thus, we likely underestimate the total outflow momentum by at least 10% (Xu et al. 2020b).

The correlation between the outflow kinetic energy and the number of YSOs in the four clouds is similar to that of mass, as shown in Figure 13.

3.4. Quantifying the Impact of Feedback with Turbulent Statistics

Feedback, including stellar winds and outflows, injects kinetic energy into the host cloud. The input energy influences the shape of the spatial power spectrum (SPS) of the integrated intensity map of ¹²CO. Xu et al. (2020a) found that stellar-wind–generated bubbles flatten the SPS of the ¹³CO integrated intensity map, which indicates that mass and energy are injected at small scales. In this section, we investigate how protostellar outflows affect the SPS of the ¹²CO integrated intensity maps.

The SPS is defined as the square of the 2D Fourier transform of an image:

$$\mathcal{P}(k) = \sum_{|\mathbf{k}|=k} |\mathcal{M}_0(\mathbf{k})|^2$$
$$= |\int_{-\infty}^{\infty} \int_{-\infty}^{\infty} M_0(\mathbf{x}) e^{-2\pi i j \mathbf{k} \mathbf{x}} d\mathbf{x}|^2, \tag{5}$$

where \mathcal{M}_0 is the zeroth moment (integrated intensity) of ¹²CO.

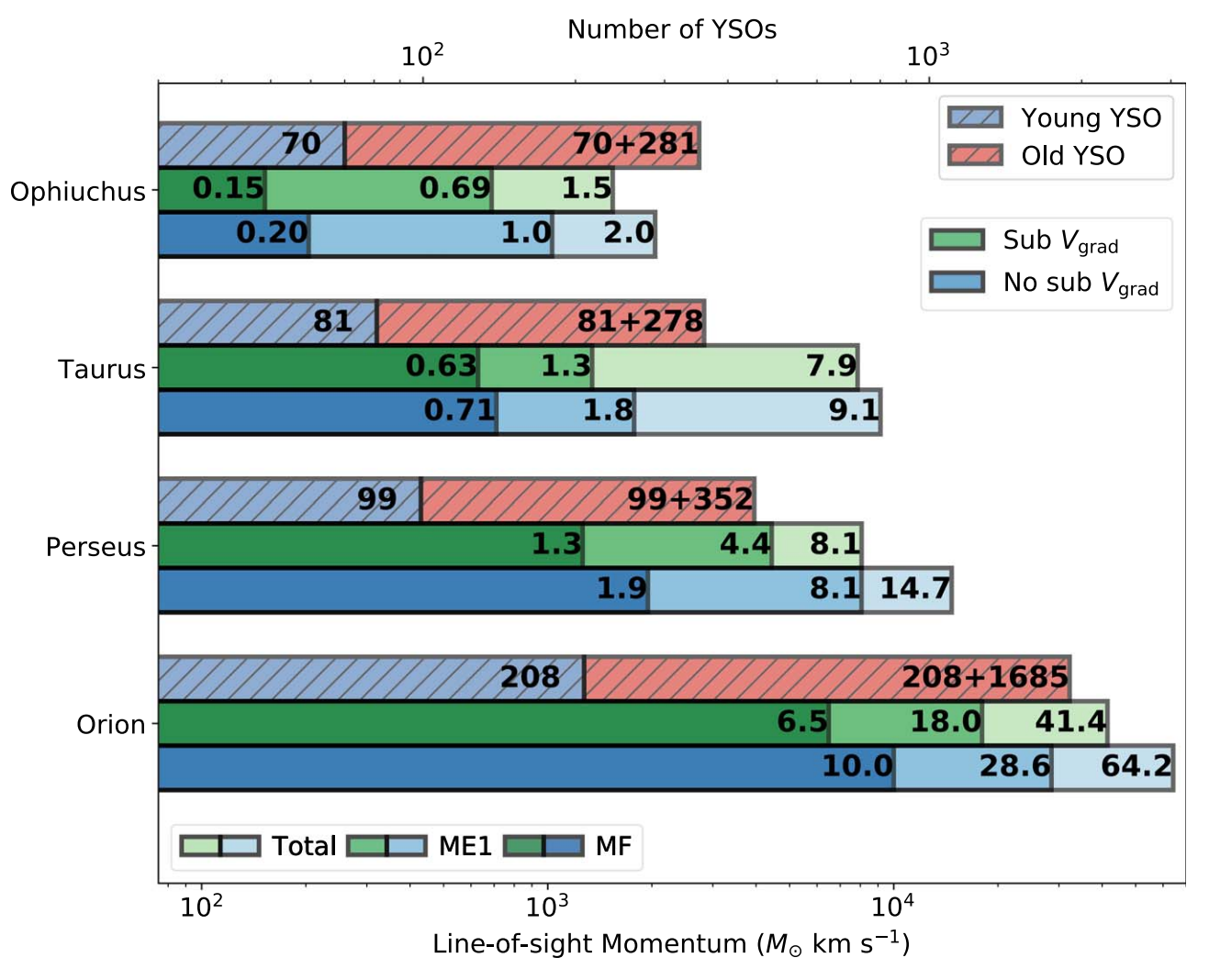


Figure 11. Outflow LOS momentum (solid colors) and the number of YSOs (hatched colors) in the four molecular clouds. Numbers in the hatched bars indicate the number of YSOs. Numbers in the unhatched bars indicate the gas momentum in units of $10^3~M_\odot~km~s^{-1}$. The total momentum indicates the momentum of the host cloud within the area studied.

Figure 14 shows the SPS of Taurus where the emission is above 0.2 K (i.e., excluding noise) and the SPS of the model ME1 and MF predicted feedback regions. Figure 14 shows that the SPS of the feedback predictions breaks into two power laws. The break point corresponds to a physical scale of ~ 0.5 pc, which might indicate the typical outflow mass and energy injection scale. For reference, we show the scale bar of this injection length in a subregion of Taurus in Figure 14. This outflow injection scale is comparable to the typical outflow size in Taurus.

We find similar broken power laws in Ophiuchus, Perseus, and Orion. We list the SPS fits for all four regions in Table 1. For a given cloud, we find the model ME1 break point scale to be similar and usually slightly higher than that of the model MF. Table 1 also lists the median of the distance between young YSOs and their four nearest young companions.

There are several competing effects that likely influence the location of the break point. For isolated outflows, the break point size is close to the outflow physical scale. However, the typical outflow size is not necessarily the same in all regions. It is influenced by the gas density and how readily the outflow can expand, as well as the source mass and age. In very clustered regions, outflows interact with each other, since the

separation between sources is smaller. This causes the outflow emission to blend together, which increases the break point.

The physical scale of the break point is small for Orion and Ophiuchus, and Taurus has an intermediate break point scale, while Perseus has the largest. Among the four clouds, Taurus has the most distributed and least clustered YSOs. Taurus also has the lowest average gas density. The mass/energy injection scale in Taurus reflects the physical size of individual molecular outflows. In Orion and Ophiuchus, the average distance between stars is small, which increases the probability that outflows from different sources interact. The mean gas densities are also higher, and high external pressure from the surrounding gas may also act to limit the propagation of outflows. For example, Kirk et al. (2017) found that all dense cores in Orion are pressure confined. All of these effects help to explain the relatively small mass/energy injection scale.

The physical scale of the break point in Perseus is significantly larger than that of the other regions. This might be due to both its typical density, which is lower than that of Orion and Ophiuchus, and the presence of multiple clusters in Perseus. Perseus hosts several intermediate-mass star-forming clusters, such as NGC 1333 and IC348. Outflows in these clusters interact and blend together, such that mass/energy

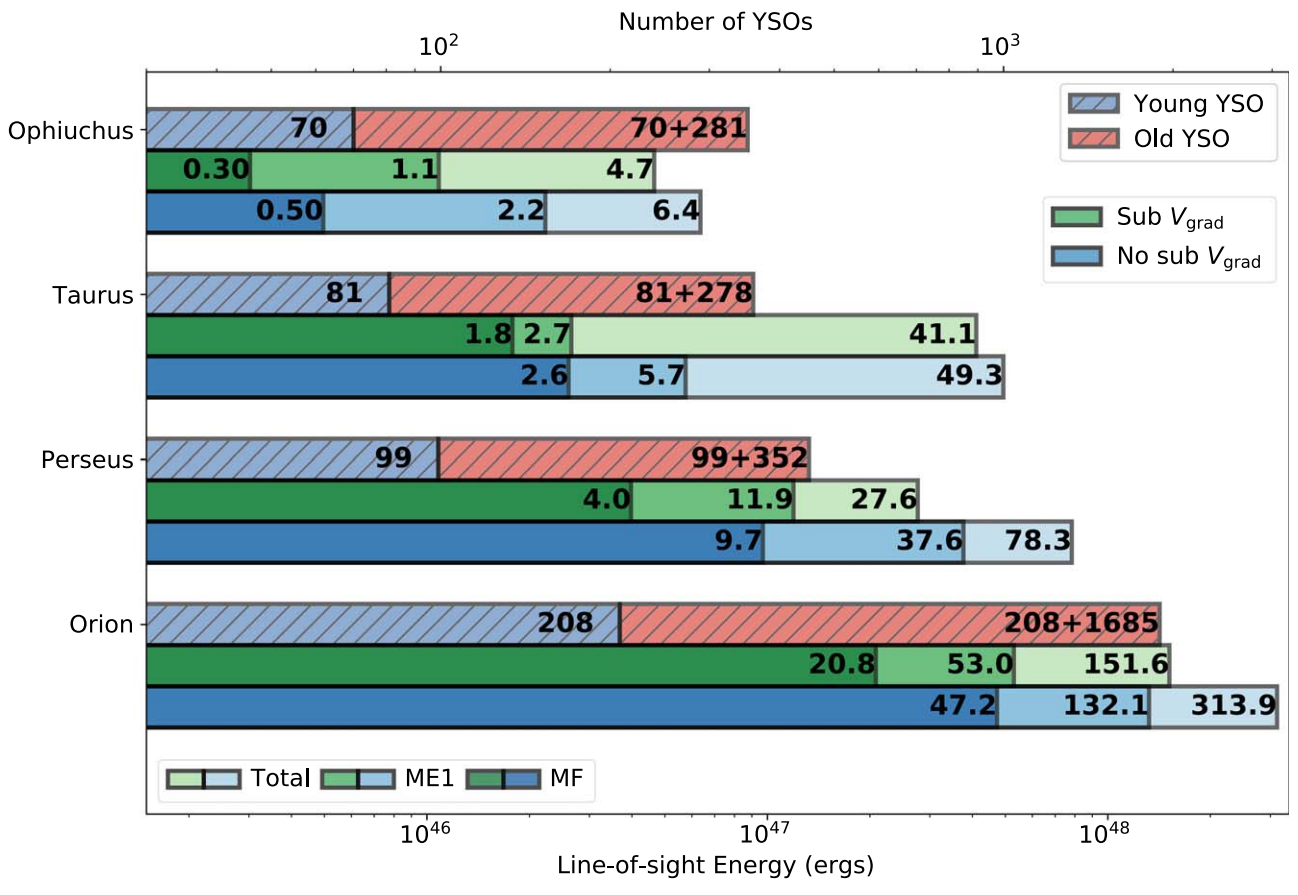


Figure 12. Outflow LOS kinetic energy (solid colors) and the number of YSOs (hatched colors) in the four molecular clouds. Numbers in the hatched bars indicate the number of YSOs. Numbers in the unhatched bars indicate the kinetic energy in units of 10⁴⁶ erg. The total energy indicates the energy of the host cloud within the area studied.

 Table 1

 Fitting Results of the Spatial Power Spectrum

Cloud	Full Map ^a Slope	ME1 ^b		MF^{b}		Young YSO
		Slope	Break (pc)	Slope	Break (pc)	Seperation ^c (pc)
Ophiuchus	-3.17 ± 0.02	$-2.47 \pm 0.05 \\ -3.71 \pm 0.07$	0.36	$-1.82 \pm 0.05 \\ -3.78 \pm 0.08$	0.38	0.24
Taurus	-2.92 ± 0.02	$-1.59 \pm 0.02 \\ -3.26 \pm 0.04$	0.56	$-1.49 \pm 0.02 \\ -3.47 \pm 0.04$	0.49	0.85
Perseus	-3.07 ± 0.02	$-2.18 \pm 0.04 \\ -3.40 \pm 0.06$	1.03	$-2.21 \pm 0.03 \\ -3.47 \pm 0.05$	0.65	0.31
Orion	-2.95 ± 0.02	-2.29 ± 0.03 -3.75 ± 0.05	0.36	-2.06 ± 0.03 -4.83 ± 0.05	0.27	0.22

Notes.

injection occurs on a relatively larger scale compared to individual stars. The average young YSO separation is slightly larger in Perseus than that in Orion and Ophiuchus, in part because the two main clusters contain few young YSOs. Consequently, the combination of these effects may explain the large mass/energy injection scale in Perseus.

To investigate how YSO clusters affect the SPS break point, we conduct an SPS analysis toward two star clusters, NGC1333 in Perseus and L1688 in Ophiuchus. We adopt different window sizes to explore the location of the break point in the cluster when viewed on different size scales. When the window size is smaller than the cluster size, we find there is

^a Single power-law fit results for the spatial power spectra for the emission regions (excluding noise).

^b Broken power-law fit results for the spatial power spectra applied to the ME1 and MF feedback maps.

^c Median of the separation between YSOs and their four nearest companions.

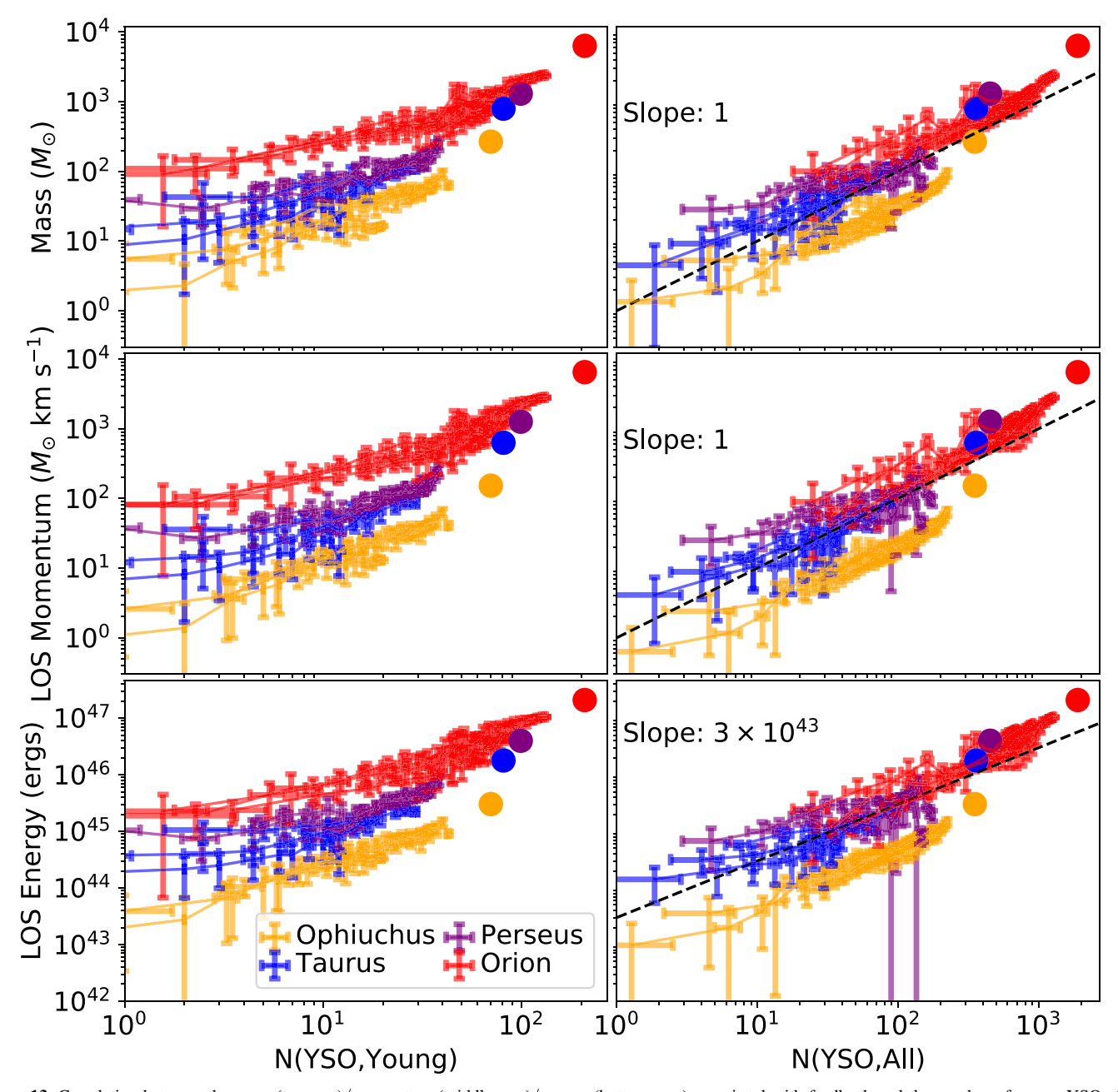


Figure 13. Correlation between the mass (top row)/momentum (middle row)/energy (bottom row) associated with feedback and the number of young YSOs (left panel) or the number of all YSOs (right panel) in the four clouds. The filled circles indicate the total outflow mass (top row)/momentum (middle row)/energy (bottom row) and the total number of YSOs (young YSOs in the left panel, all YSOs in the right panel) in the four clouds. The window sizes are $0.5 \text{ pc} \times 0.5 \text{ pc}$, $1 \text{ pc} \times 1 \text{ pc}$, and $2 \text{ pc} \times 2 \text{ pc}$ for Ophiuchus, and $2 \text{ pc} \times 2 \text{ pc}$, $3 \text{ pc} \times 3 \text{ pc}$, and $5 \text{ pc} \times 5 \text{ pc}$ for Taurus and Orion. The window sizes for Perseus are $2 \text{ pc} \times 2 \text{ pc}$ and $3 \text{ pc} \times 3 \text{ pc}$.

no break point in the SPS for both clustered regions, and the slope is steeper. When the window size is two or more times larger than the cluster size, the break point appears. However, the break point scale is not neatly correlated with the size of the cluster nor the window size. NGC1333 has a break point between 0.6 and 0.7 pc, while L1688 has a break point scale between 0.3 and 0.4 pc. These scales are similar to those of the full predictions, which suggests that the outflows in the clustered regions are influencing the location of the overall break point.

We also explore the effect of different observation resolutions on the results. The observations of Ophiuchus, Taurus, and Orion have a similar physical scale per pixel, 0.013–0.015 pc pixel⁻¹. However, the physical scale per pixel

of Perseus is twice that of the others. We convolve the Ophiuchus and Orion observations to a similar effective resolution as Perseus, and apply the CASI-3D models to these convolved data cubes and conduct the same SPS analysis on the convolved data. However, we find only minor changes in the break point. For example, the break point remains the same in the convolved Ophiuchus model MF prediction and increases by 0.1 pc in the convolved Ophiuchus model ME1 prediction. However, it decreases by 0.08 pc in the convolved Orion ME1 prediction, while increasing by 0.08 pc in the Orion MF prediction. We find no significant trend when convolving with a larger beam and conclude the analysis is relatively insensitive to the resolution. However, this test suggests that the break point has an uncertainty of ± 0.1 pc, which is smaller

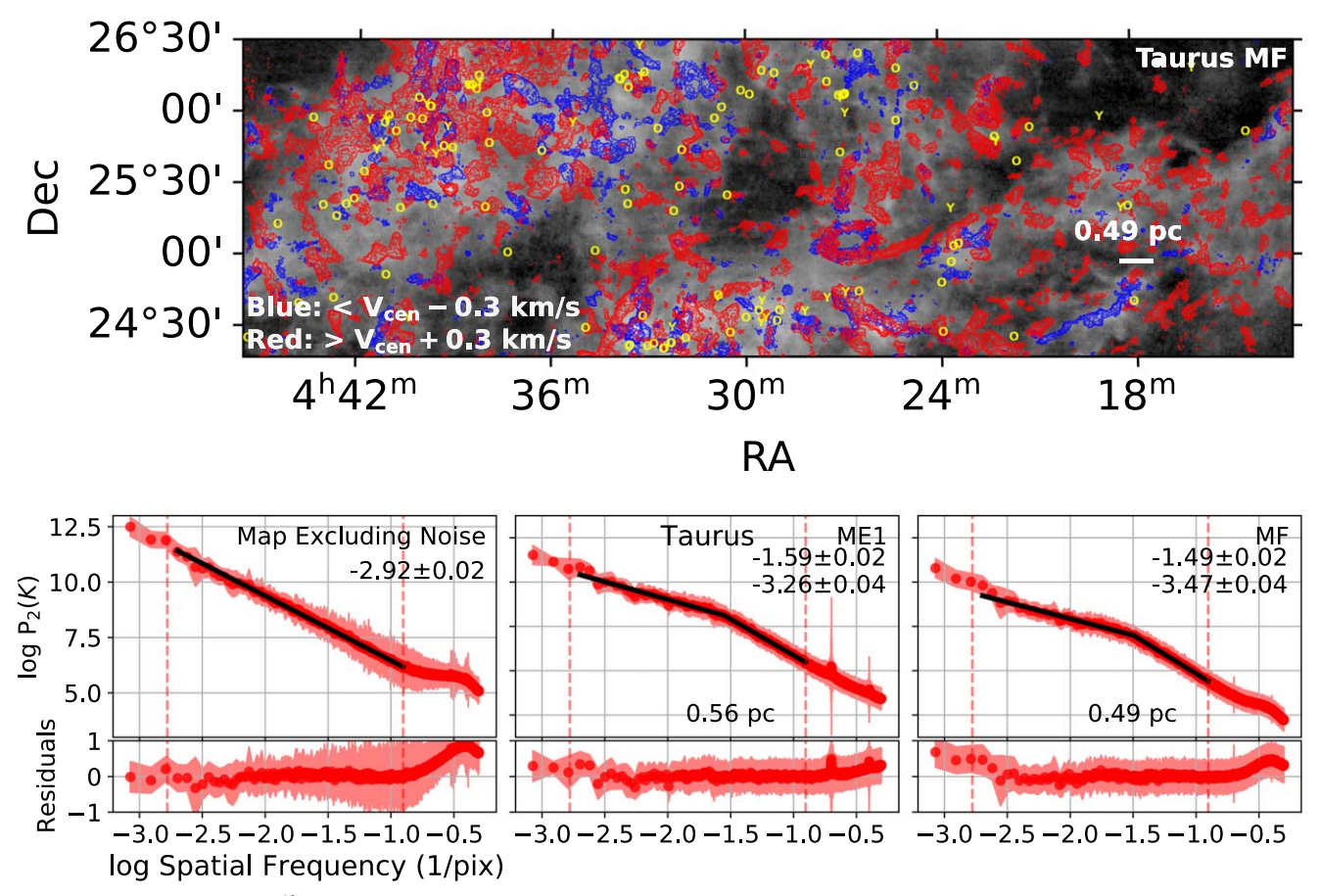


Figure 14. Upper panel: intensity of ¹²CO (1–0) integrated over all velocity channels for a subregion in Taurus, overlaid with the model MF prediction (red and blue contours). The physical scale of the break point in the SPS is also shown for reference. Lower panels: the spatial power spectrum (SPS) of the regions in Taurus where the emission is above 0.2 K (excluding noise) and the SPS of the model ME1 and MF predicted feedback regions. The top right number in each panel indicates the slope of the fit. The middle bottom number in each panel indicates the physical scale of the broken point.

than the difference between the break point of Perseus and those of the other clouds.

Finally, to test whether (non-feedback) gas structures influence the break point location, we compute the SPS for the dense regions of the clouds that are traced by ¹³CO. We mask out the low-intensity pixels to isolate only the dense gas. We compare the results for two clouds, Orion and Taurus. When all pixels with intensities below 5 K are removed, there is no break point in the Orion SPS. For the densest regions, i.e., as defined using an intensity cut-off of 10 K, we find a break point at 0.6 pc. This is two times larger than that of the break point of the outflow maps. We find a similar result in Taurus. When applying a high-intensity cut-off, we find a break point around 1 pc, which is a size-scale twice that of the break point identified by the Taurus SPS outflow analysis. We conclude that our outflow predictions are not correlated with dense cloud structures.

4. Discussion

4.1. Outflows without Driving Sources and False Detections

Confirming outflow identifications requires ancillary data, e.g., YSO catalogs. With the help of YSO locations, we are able to increase confidence in the CASI-3D predictions, which are based on ¹²CO data only. In this section, we discuss two cases predicted by CASI-3D: a region in Taurus with no detected YSOs, and a region in Orion with no young YSOs.

Figure 15 presents the channel-by-channel prediction by model MF on a region with no YSOs in Taurus. This region is considered to be a trans-Alfvenic flow regulated by magnetic fields (Heyer & Brunt 2012; Heyer et al. 2016), which has low surface brightness ¹²CO emission. There are no known YSOs observed by GAIA or Herschel (Roccatagliata et al. 2020). Consequently, we believe there is no outflow activity. However, the model MF predicts outflow activity in this region. Inspection of the channel map shows that a coherent jet-like structure exists across several velocity channels. These structures actually visually resemble outflows, which might be the reason for the model failure.

Figure 16 shows the model MF prediction along a position-velocity cut of the fake outflow in Figure 15. In the position-velocity diagram, we identify two faint coherent high-velocity blobs between 4 and 5 km s⁻¹. Their morphology is similar to some of the faint outflows (e.g., TMO22 in Li et al. 2015). Since these ¹²CO structures are indistinguishable from true outflows, CASI-3D is not able to recognize these false detections based only on ¹²CO morphology. In terms of morphology, CASI-3D performs robustly in identifying coherent high-velocity features that are similar to outflows. But many mechanisms may cause coherent high-velocity features, including but not limited to cloud formation, cloud–cloud collision, gas phase transition near the cloud boundary, or gas flows regulated by MHD waves (Heyer & Brunt 2012; Motte et al. 2014; Nakamura et al. 2014; Heyer et al. 2016).

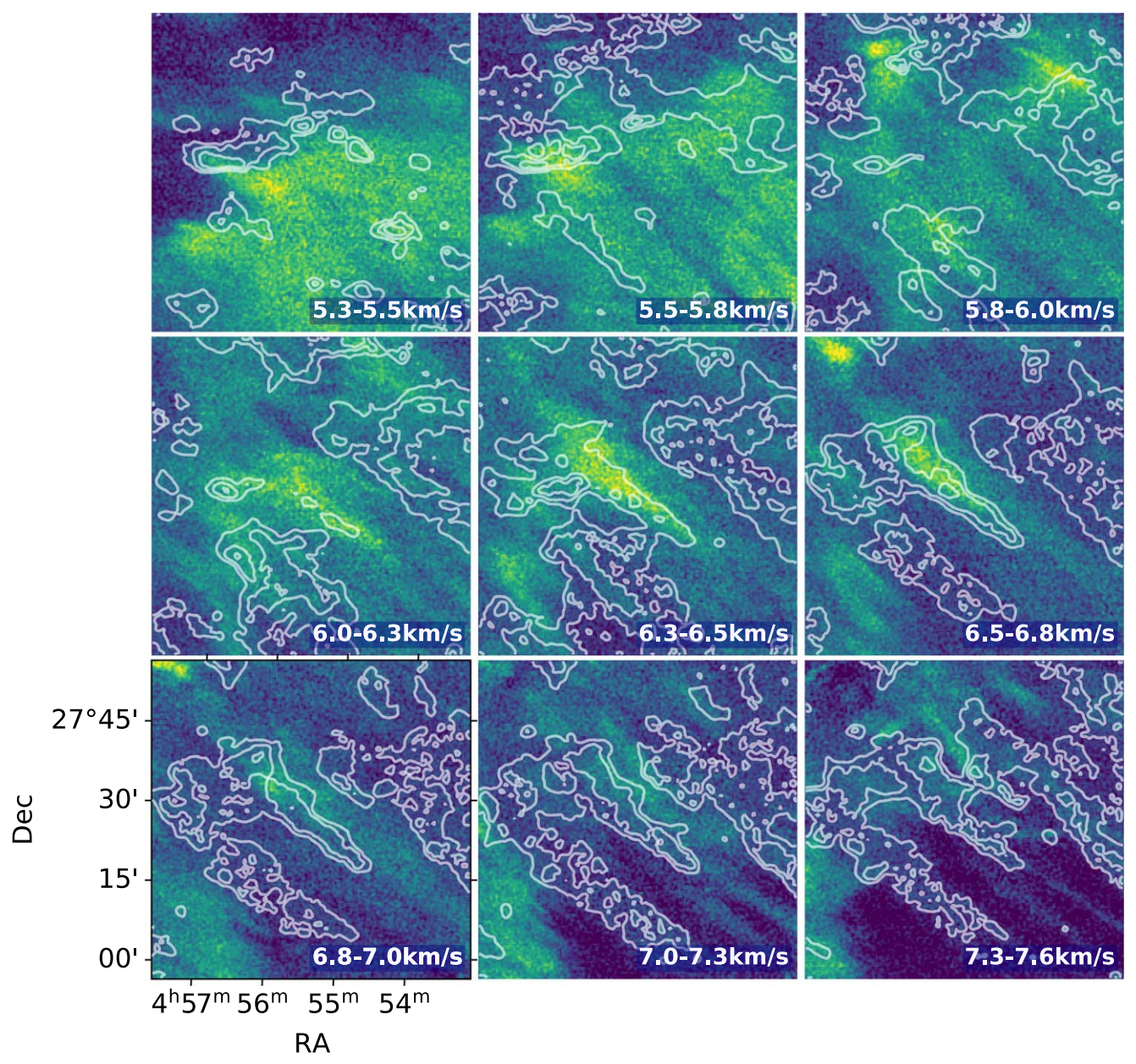


Figure 15. ¹²CO channel map of a region with no YSOs in Taurus overlaid with the prediction by the model MF in white contours.

Figure 17 shows an example of the performance of models ME1 and MF toward a region where there are no young YSOs in Orion. In the position-velocity diagram, we identify a clear outflow-like feature above $10\,\mathrm{km\,s^{-1}}$, which is also identified by the two models. We notice that there are several old evolutionary stage YSOs nearby, which might act as driving sources. One reason might be that the boundary between young and old is not so well defined, which is discussed in Section 3.3. Or these outflow structures might exist for a much longer timescale than that of their driving sources. We recognize that there are two velocity components in the molecular cloud at this position. A narrow gas bridge located around 8 km s⁻¹ connects these two gas components, which is likely an outflow. We cannot confirm the origin of this highvelocity component. It might be caused by the fossil outflows from YSOs or by two converging gas flows. All of these mechanisms cause similar high-velocity features, which cannot be easily distinguished either visually or using CASI-3D.

In order to validate that our CASI-3D models are sensitive to gas velocity structures and morphology but not only the dense regions, we examine the CASI-3D performance on several previously identified filaments in Taurus. Panopoulou et al. (2014) identified 10 filamentary structures in ¹³CO emission in Taurus, and illustrated the PPV diagrams of the filaments in Figure 15 in their paper. The filaments have very coherent motions and exhibit small velocity dispersions. Their filaments 3, 4, 5, 6, and 7 do not have significant high-velocity components. When comparing with our outflow predictions (Figures 4 and 5 in this work) and bubble predictions (Figures 17 and 18 in Xu et al. 2020a), we find that both models predict little feedback along these filaments. However, when we look at Filament 2 (also known as L1495/B213), we see a clear high-velocity structure with a "U" shape. This morphology is consistent with the theoretical bubble morphology shown in Figure 5 in Arce et al. (2011). Unsurprisingly, both CASI-3D models that identify bubbles and outflows predict the presence

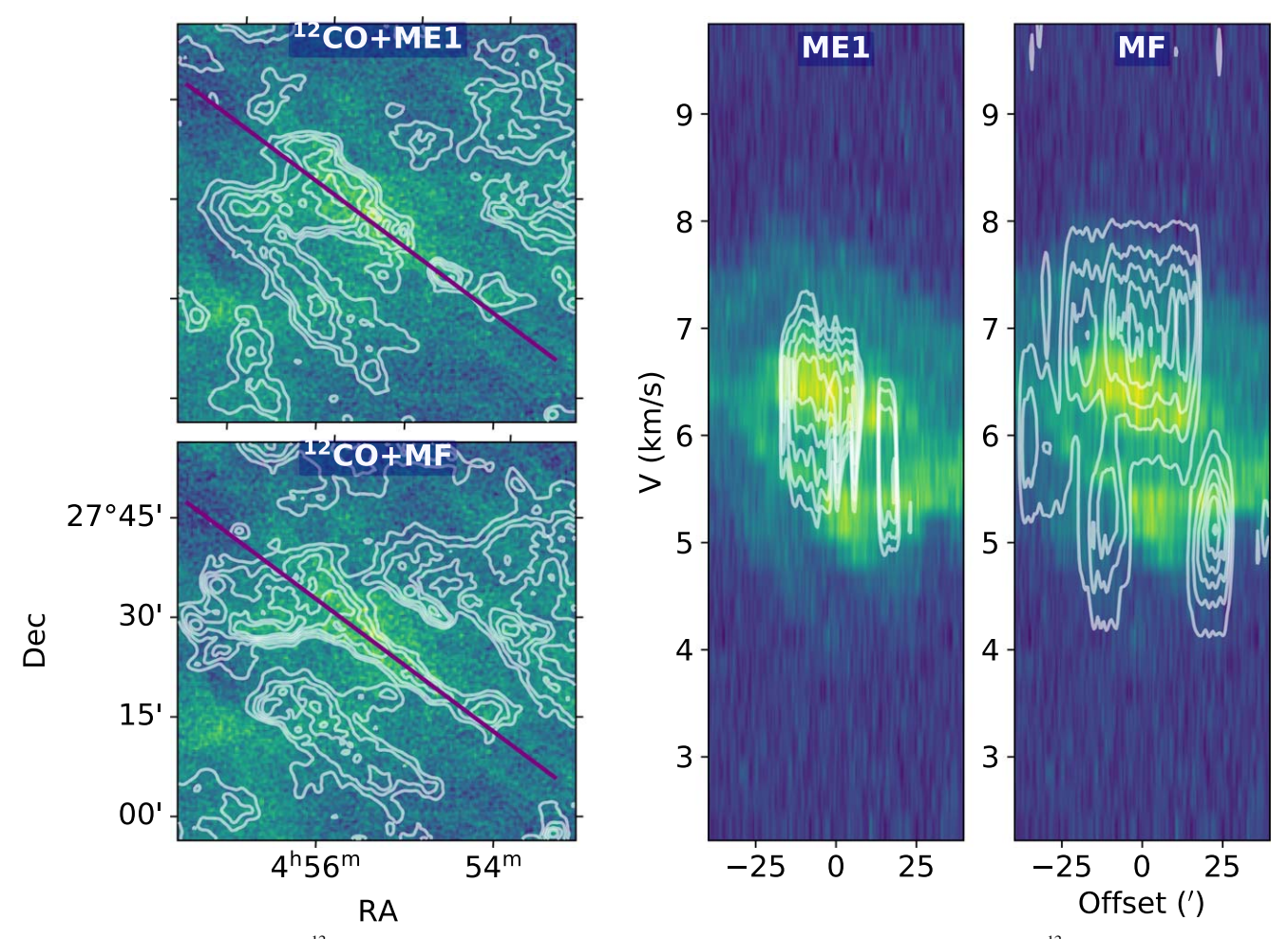


Figure 16. Position–velocity diagram of ¹²CO emission toward a region with no YSOs in Taurus. Left panel: integrated intensity of ¹²CO over the full velocity range (from -1.5 to 13.4 km s^{-1}) overlaid with the model ME1 and MF predictions in white contours. The purple line illustrates the cut direction of the position–velocity diagram. Middle and right panel: position–velocity diagram of ¹²CO emission overlaid with the model ME1 and MF predictions in white contours.

of feedback at the location of filament 2. CASI-3D may return a false detection if the morphology of a structure is similar to that of outflows or bubbles. In this case, visual inspection suggests that filament 2 also contains a bubble, so it is likely that the feedback identified by our models at this location is real. We emphasize that machine-learning models are not perfect tools. They must be applied with caution and checked thoroughly.

4.2. Outflows versus Bubbles

In this section we investigate the overlap between a model identifying outflow feedback and one identifying stellar-wind feedback. We present the prediction by two sets of models: those trained to identify protostellar outflows and those trained to identify stellar-wind-driven bubbles.

The morphology of bubbles is more symmetric and arc-like compared to that of outflows. However, when the line of sight is parallel to an outflow launching axis, i.e., looking through the cavity of the outflow, the morphology of the outflow can resemble that of a bubble. Figure 18 illustrates an example of a synthetic outflow whose launching axis is parallel to the line of sight. Consequently, models trained to identify outflows are likely to also identify some bubble structures.

Figure 19 shows the prediction by models trained to identify stellar-wind-driven bubbles toward Ophiuchus L1688 Region. Comparison with Figure 3 shows that the prediction by models

trained to identify protostellar outflows covers most of the regions that are identified as bubbles. Quantitatively, 68% of the voxels are identified as feedback by both MF models, 21% of the voxels are identified as only outflow feedback, while 11% of the voxels are identified as only belonging to bubbles. Statistically, we might neglect 13% of the feedback gas associated with stellar winds when adopting the mass estimates predicted by models trained to identify protostellar outflows. On average, the outflow mass predicted by models can serve as a decent estimate for feedback mass.

To better investigate the difference between outflows and bubbles, we employ an unsupervised learning method t-SNE (tdistributed Stochastic Neighbor Embedding) to study the similarities between the spectra of outflows and those of bubbles. We discuss t-SNE and the results in detail in Appendix B. Our main finding is that there is a variation in spectra shape for outflows and bubbles. And even the spectra that are dominated by outflow gas show various spectral shapes. Meanwhile, there are some "transitional spectra" with a shape similar to both. We note that the t-SNE representation encodes only 1D information about the spectra and does not represent any correlations in the spatial dimension. Consequently, this analysis provides intuition for understanding the features that the models select when they identify feedback, and it illustrates the challenge of distinguishing outflows and bubbles based only on the LOS spectrum.

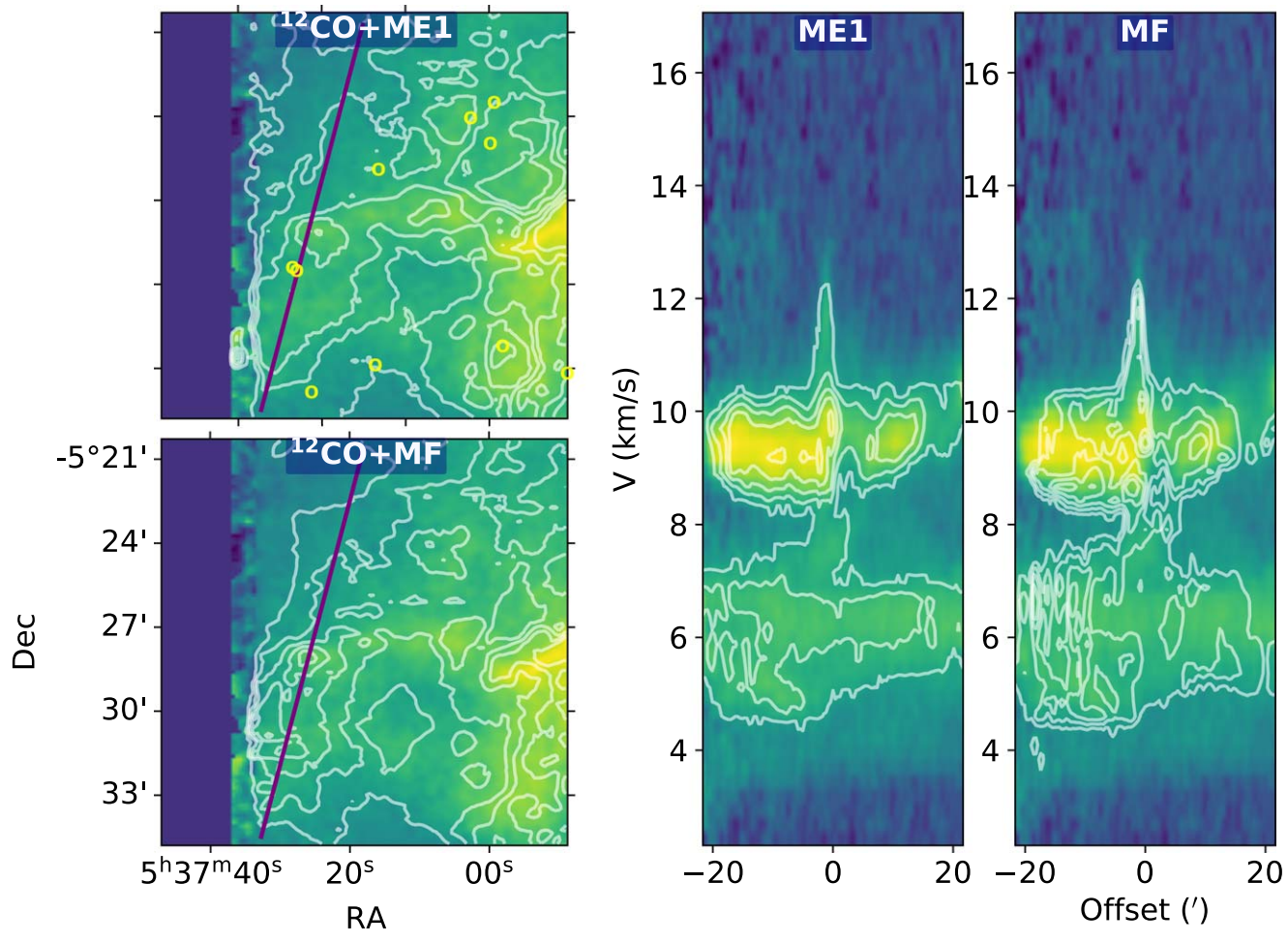


Figure 17. Position–velocity diagram of ¹²CO emission toward a region without young YSOs in Orion. Left panel: integrated intensity of ¹²CO over the full velocity range (from 2.3 km s⁻¹ to 17.1 km s⁻¹) overlaid with the model ME1 and MF predictions in white contours. Letters "O" mark old YSO positions. The purple line illustrates the cut direction of the position–velocity diagram. Middle and right panel: position–velocity diagram of ¹²CO emission overlaid with the model ME1 and MF predictions in white contours.

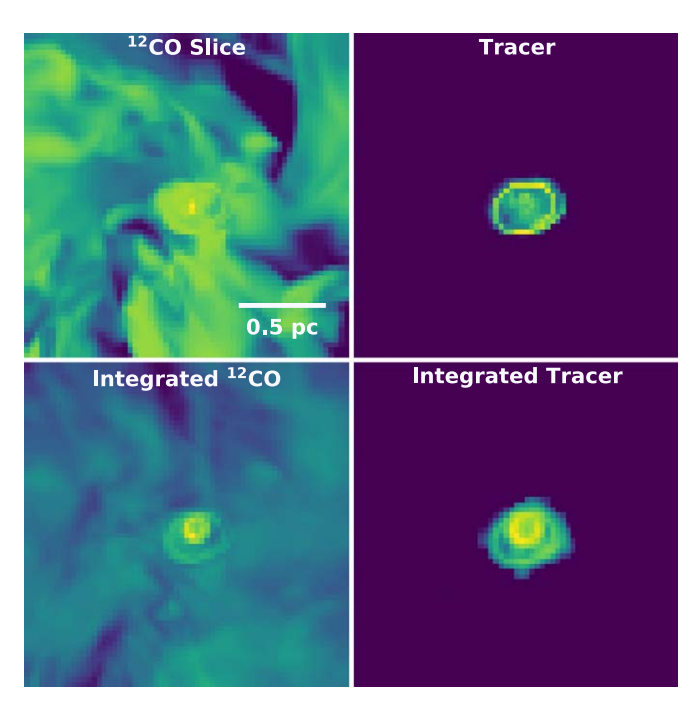


Figure 18. A synthetic outflow whose launching axis is parallel to the line of sight.

4.3. Impact of Outflows on Molecular Clouds

In this section, we place our energy estimations (Section 3.2) in the context of prior work and discuss the broader implications of the global impact of outflows. Most prior work derives the total outflow energy by assuming a moderate inclination angle and multiplying the 1D energy estimate by a factor of three. For example, Dunham et al. (2014a) adopted an inclination angle of 57.13, which yields an energy correction factor of 3.4. Here we make the same assumption and report the 3D total, where we multiply our 1D estimate by a factor of three.

To investigate the impact of outflows on turbulence, a typical approach is to compare the turbulence dissipation rate and the outflow energy injection rate (e.g., Arce et al. 2010; Li et al. 2015; Feddersen et al. 2020). However, the outflow energy injection timescale is highly uncertain. As discussed in Section 3.3, we find the outflow mass is linearly correlated with the total number of YSOs instead of only the younger sources, which indicates that the driving timescale of outflows is even less clear. Instead, we compute the total outflow kinetic energy—a quantity estimated as part of previous analyses in the determination of the outflow injection rate—and compare our new values to those in the prior published studies. This allows

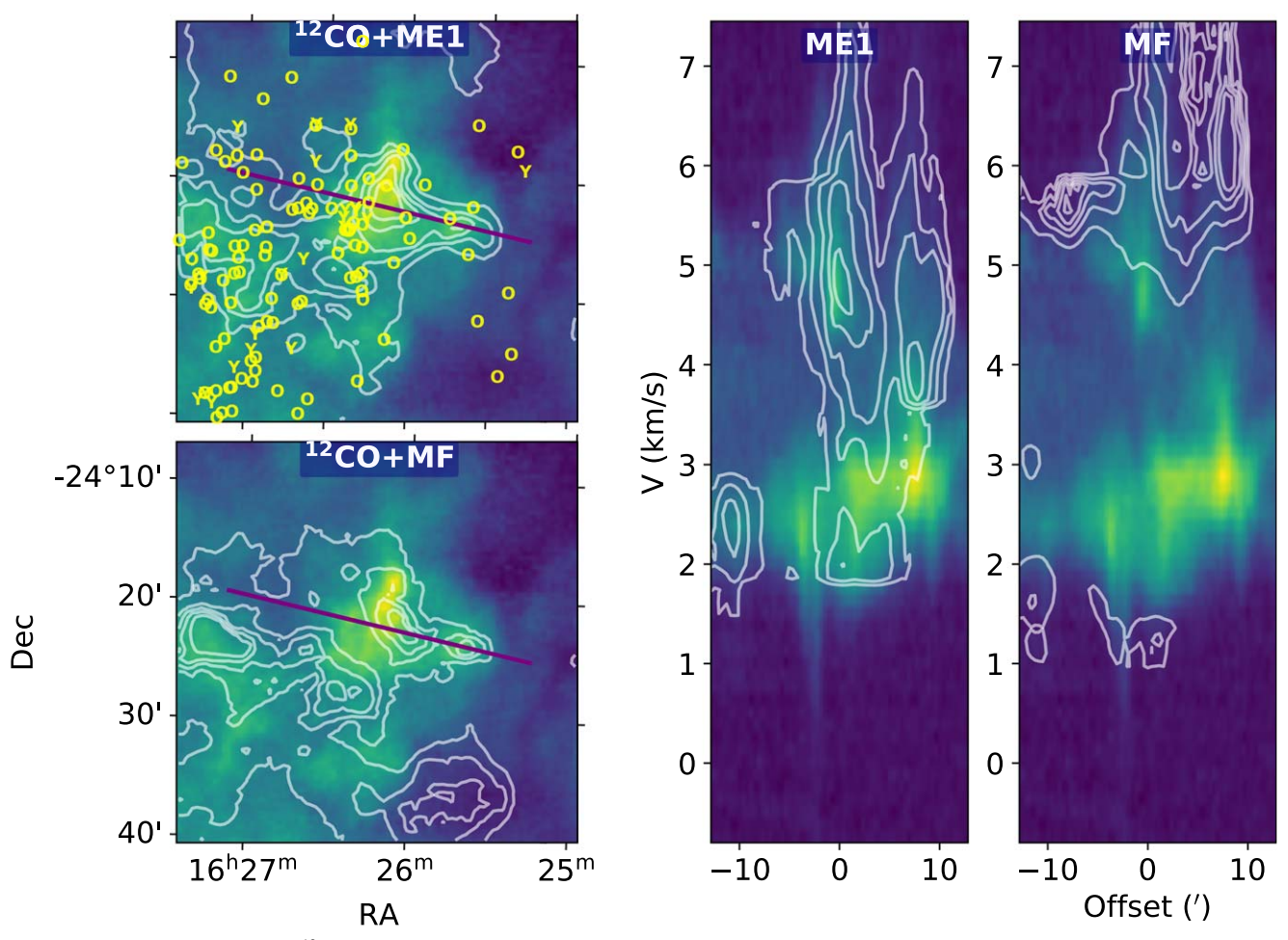


Figure 19. Position–velocity diagram of ¹²CO emission toward Ophiuchus L1688 Region, similar to Figure 3 but predicted by models trained to identify stellar-wind-driven bubbles

us to conclude whether the impact of outflows is relatively similar to, more or less, that in prior analyses.

Nakamura et al. (2011) conducted observations of ¹²CO (3–2) and ¹²CO (1–0) toward an active cluster-forming clump in Ophiuchus and identified six molecular outflows in both data. Nakamura et al. (2011) derived the outflow mass from ¹²CO (3-2) and ¹²CO (1-0) emission located in the highvelocity line wings. They derived a total outflow kinetic energy of 6×10^{44} erg. After comparing the total outflow energy injection rate with the dissipation rate of the supersonic turbulence, Nakamura et al. (2011) concluded that outflows inject significantly more energy than needed to offset the dissipation of turbulence. In our work, we find that the total outflow kinetic energy is 9×10^{45} erg, which is an order of magnitude larger than the value in Nakamura et al. (2011). A larger area coverage in our work and using the optically thin tracer ¹³CO in mass estimates might explain this difference. ¹²CO (3–2) and ¹²CO (1–0) are likely optically thick, which could cause their outflow mass, momentum, and energy to be underestimated. More importantly, our method does not discard the outflow material ejected perpendicular to the line of sight that is located near the cloud central velocity. Since our energy calculation leads to a higher energy estimate, our result confirms the conclusion that outflow kinetic energy is sufficient to compensate for the dissipation of turbulence in Ophiuchus.

Li et al. (2015) conducted a feedback census in Taurus and identified 55 outflows and 37 bubbles. They derived a total

outflow energy of 3.9×10^{45} erg, which is 1% of the Taurus cloud turbulent energy. However, Li et al. (2015) found that bubbles dominate the feedback energy. When also combining the kinetic energy from bubbles, they found the total kinetic energy from stellar feedback in Taurus is 30% of the cloud turbulent energy. Since the energy injection rate from stellar feedback is comparable to the dissipation rate of the cloud turbulence, they concluded that stellar feedback, mainly in the form of bubbles, is sufficient to maintain turbulence in the current epoch. However, Xu et al. (2020a) showed that the Li et al. (2015) bubble energy estimate was substantially overestimated due to LOS contamination, which is caused by gas emission that is not associated with feedback being included in the outflow/bubble estimate. After correction, the kinetic energy from bubbles decreased by a factor of four. In our current work, we find the total outflow kinetic energy is 5.4×10^{46} erg, which is an order of magnitude larger than the value in Li et al. (2015). This difference is likely caused by a similar reason to that in Ophiuchus, i.e., our method includes the outflow material located around the cloud central velocity that is excluded in traditional approaches. Our calculation indicates that the kinetic energy from outflows is 14% of the cloud turbulent energy. If we combine the contribution from bubbles (Xu et al. 2020a), the total kinetic energy from stellar feedback is 22% of the cloud turbulent energy. Li et al. (2015) concluded that the outflow energy injection rate is marginally comparable to the dissipation rate of turbulence in Taurus,

although outflow energy is only 1% of the Taurus cloud turbulent energy. With our updated feedback energy, which is 22% of the cloud turbulent energy, we conclude that the feedback energy injection rate can compensate for the turbulent dissipation rate (Li et al. 2015; Xu et al. 2020a).

Arce et al. (2010) identified 60 outflow candidates in Perseus and derived a total outflow energy of 2×10^{46} erg, which is 12.5% of the total cloud turbulent energy. However, it is worth noting that the method of calculating cloud turbulent energy used in Arce et al. (2010) is different from our method. Arce et al. (2010) adopted an average line width of 2 km s⁻¹ to calculate the turbulent energy. While in this work, we calculate the turbulent energy channel by channel followed by Equation (3). The cloud turbulent energy derived by Arce et al. (2010) is 1.6×10^{47} erg, while our approach indicates an estimate of 8×10^{47} erg, which is a factor of five larger than the estimate by Arce et al. (2010). To make a fair comparison, we adopt our turbulent energy estimate to discuss the impact of outflows in Perseus. Under these circumstances, the kinetic energy of the previously identified outflows are only 2.4% of the total cloud turbulent energy. Xu et al. (2020b) applied CASI-3D to the same outflow catalog and predicted a total outflow energy of 7.8×10^{45} erg, which is onefourth of the value in Arce et al. (2010). This is caused by the lower mass-weighted LOS velocity as discussed in Section 3.3. In our present work, we derive a total outflow energy of 1.2×10^{47} erg, which is six times larger than that in Arce et al. (2010). There are several possible reasons for this higher value. First, there are newly identified isolated outflows as discussed in Xu et al. (2020b). It should be noted that Xu et al. (2020b) just followed up the 60 previous outflows and identified a few new outflows in the vicinity of these, whereas our current work makes a prediction using the full CO map, which includes the entire cloud and a couple of clusters. This likely increase the outflow kinetic energy by a factor of a few. Second, CASI-3D is able to identify all feedback structures in clustered regions, which are not fully identified in previous works. This also may enlarge the outflow energy by a factor of a few. Moreover, outflows identified by Arce et al. (2010) are all distinct outflows with obvious coherent highvelocity structures that are likely powered by strong driving sources. However, in our work, CASI-3D also identifies less distinct outflows whose velocities are small compared to previously identified ones. These weaker, less distinct outflows might be driven by more evolved or lower-mass sources. This indicates that CASI-3D provides a more inclusive outflow sample. Arce et al. (2010) concluded that the 60 outflow candidates they identified play an important role in maintaining turbulence at the current epoch in Perseus, although the kinetic energy of outflows is 12.5% of the total cloud turbulent energy in their study, or 2.4% of the total cloud turbulent energy in our turbulence calculation. However, our updated outflow kinetic energy estimate is 15% of the cloud turbulent energy. This indicates that outflows still play an important role in maintaining turbulence in Perseus.

Feddersen et al. (2020) identified 45 outflows near Herschel Orion Protostar Survey protostars (Furlan et al. 2016) in Orion but skipped the OMC-1 region. They derived a total outflow energy of $0.7-1.7 \times 10^{46}$ erg. They found that the total outflow energy injection rate is comparable to the dissipation rate of turbulence. In our work, we derive a total outflow energy of 2.1×10^{47} erg, which is an order of magnitude larger than previous estimates. The main reason for the difference is that our survey covers a larger area and does not only focus on gas near the position of YSOs. In particular, we include the most active star-forming

region OMC-1. CASI-3D predicts the kinetic energy from outflows in OMC-1 is 7.7×10^{46} erg, which is 37% of the entire outflow energy in Orion. Thus, we confirm the prior conclusion that outflows are sufficient to maintain turbulence in Orion.

In conclusion, our outflow kinetic energy estimates for all four clouds are larger than previous estimates. Consequently, we confirm the previous conclusion that outflows are an important agent to maintain turbulence at the current epoch.

4.4. Uncertainties of Outflow Estimates

In Section 3.2, we calculated the masses and dynamical properties of the outflows for the four clouds. In this section, we attempt to quantify the uncertainty of these outflow estimates.

First, we assume a moderate excitation temperature of 25 K or the ¹²CO peak temperature, whichever is higher, to calculate the outflow mass. Most studies adopt values of excitation temperature in the range of 10–50 K (Dunham et al. 2014a; Feddersen et al. 2020). Since the mass scales linearly with the excitation temperature, the choice of excitation temperature introduces a factor-of-two uncertainty.

Meanwhile, Xu et al. (2020b) found that model MF predicts the outflow mass within a scatter of 0.41. The most extreme offset case over-/under- estimates the mass by a factor of two. We did not find any offset that would cause a systematic over- or underestimation. Meanwhile, we carry out one additional test to constrain the degree of possible contamination from cloud emission at rest-frame gas velocities. Appendix F shows an analysis of a more complex synthetic observation, which contains a number of interacting outflows. We conclude that our CASI-3D model is generally able to exclude contamination from the ambient gas near the rest-frame velocity and may even underestimate the outflow contribution from low velocities in complex star-forming areas.

Furthermore, high-velocity, low-density gas emission is easily missed in high-velocity channels due to the low signal-to-noise. Xu et al. (2020b) used the simulations to estimate that 10% of the outflow gas is lost. The correction factors for LOS momentum and LOS energy are 1.3 and 1.8 (Xu et al. 2020b), respectively.

In addition, the inclination angle of the outflow plays an important role in converting LOS momentum/energy to 3D momentum/energy. In this work, we adopt correction factors of $\sqrt{3}$ and 3 to convert LOS momentum and LOS energy to 3D estimates. These correspond to an inclination angle of 55°. If the inclination angle is between 20° and 70°, this leads to a factor-of-two uncertainty for 3D momentum and a factor-of-four uncertainty for 3D energy.

Finally, chemical conditions, i.e., 12 CO and 13 CO abundances, have an influence on the mass estimate. In our mass calculation, we adopt constant abundance ratios, $[^{12}$ CO]/ $[H_2] = 10^{-4}$ and $[^{12}$ CO]/ $[^{13}$ CO] = 62. However, these abundance ratios vary across diffident clouds. We cannot evaluate this uncertainty without sophisticated chemical modeling for each cloud.

Consequently, by combining these uncertainties and using error propagation, we find a factor-of-three uncertainty for mass, a factor-of-3.4 uncertainty for 3D momentum, and a factor-of-five uncertainty for 3D energy.

5. Conclusions

We apply the deep learning method CASI-3D to four nearby molecular clouds, Ophiuchus, Taurus, Perseus, and Orion, to systemically identify protostellar outflows and study the impact of outflows on their host clouds. Our main findings are as follows:

- 1. The total outflow masses are 267 M_{\odot} , 795 M_{\odot} , 1305 M_{\odot} , and 6332 M_{\odot} for Ophiuchus, Taurus, Perseus, and Orion, respectively. On average, the mass associated with feedback is around 10% of the host cloud mass for all four clouds.
- 2. The total 3D outflow energies are 9×10^{45} erg, 6×10^{46} erg, 1.2×10^{47} erg, and 6×10^{47} erg for Ophiuchus, Taurus, Perseus, and Orion, respectively.
- 3. The outflow mass is linearly proportional to the total number of YSOs for all four clouds. On average, each YSO is associated with 1 M_{\odot} of outflow material.
- 4. The outflow momentum is linearly proportional to the total number of YSOs for all four clouds. On average, each outflow has a mass-weighted LOS velocity of 1 km s⁻¹. This relatively low value is because more mass is located near the cloud central velocity.
- 5. We compute the SPS of the outflow prediction map. We find all four clouds exhibit a break point, which ranges from 0.27 pc (Orion) to 0.65 pc (Perseus). The break point likely indicates the typical outflow mass and energy injection scale.
- Models trained to identify outflows are likely to also identify bubble structures, which may be produced by main-sequence massive stars.
- 7. We compare the energy associated with outflows to the rate of turbulent dissipation and conclude that feedback is sufficient to maintain turbulent dissipation at the current epoch for all four clouds.

D.X., S.S.R.O., and R.A.G. acknowledge support by NSF grant AST-1812747. D.X. acknowledges support from the David Alan Benfield Memorial Scholarship in Astronomy and from the Virginia Initiative on Cosmic Origins (VICO). S.S.R.O. acknowledges support from NSF Career grant AST-1748571. R.A.G. acknowledges support from NASA ADAP grant NNX17AF24G. H.G.A. acknowledges support from NSF grant AST-1714710. The Texas Advanced Computing Center (TACC) at the University of Texas at Austin provided HPC resources that have contributed to the research results reported within this paper.

Appendix A Discussion on the Effect of Box Sizes on the YSO-Mass Relation

In this section, we examine the effect of our choice of "window" sizes when studying the correlation between the total mass associated with outflows and the number of YSOs. We define windows with physical sizes of $0.5 \, \mathrm{pc} \times 0.5 \, \mathrm{pc}$, $1 \, \mathrm{pc} \times 1 \, \mathrm{pc}$, $2 \, \mathrm{pc} \times 2 \, \mathrm{pc}$, $3 \, \mathrm{pc} \times 3 \, \mathrm{pc}$, and $5 \, \mathrm{pc} \times 5 \, \mathrm{pc}$ to scan through the entire cloud region. We set a step size such that each box overlaps with its neighbors by at least 80%. Then we calculate the mass inside the window and count the number of YSOs enclosed. We consider the outflow relationship between the number of both young YSOs and total YSOs.

Figure 20 shows the correlation between the model MF outflow prediction and the number of young YSOs for the five window sizes applied to the four clouds. For Ophiuchus, Perseus, and Orion, when the window size is above a certain threshold, the correlations between outflow mass and the number of YSOs

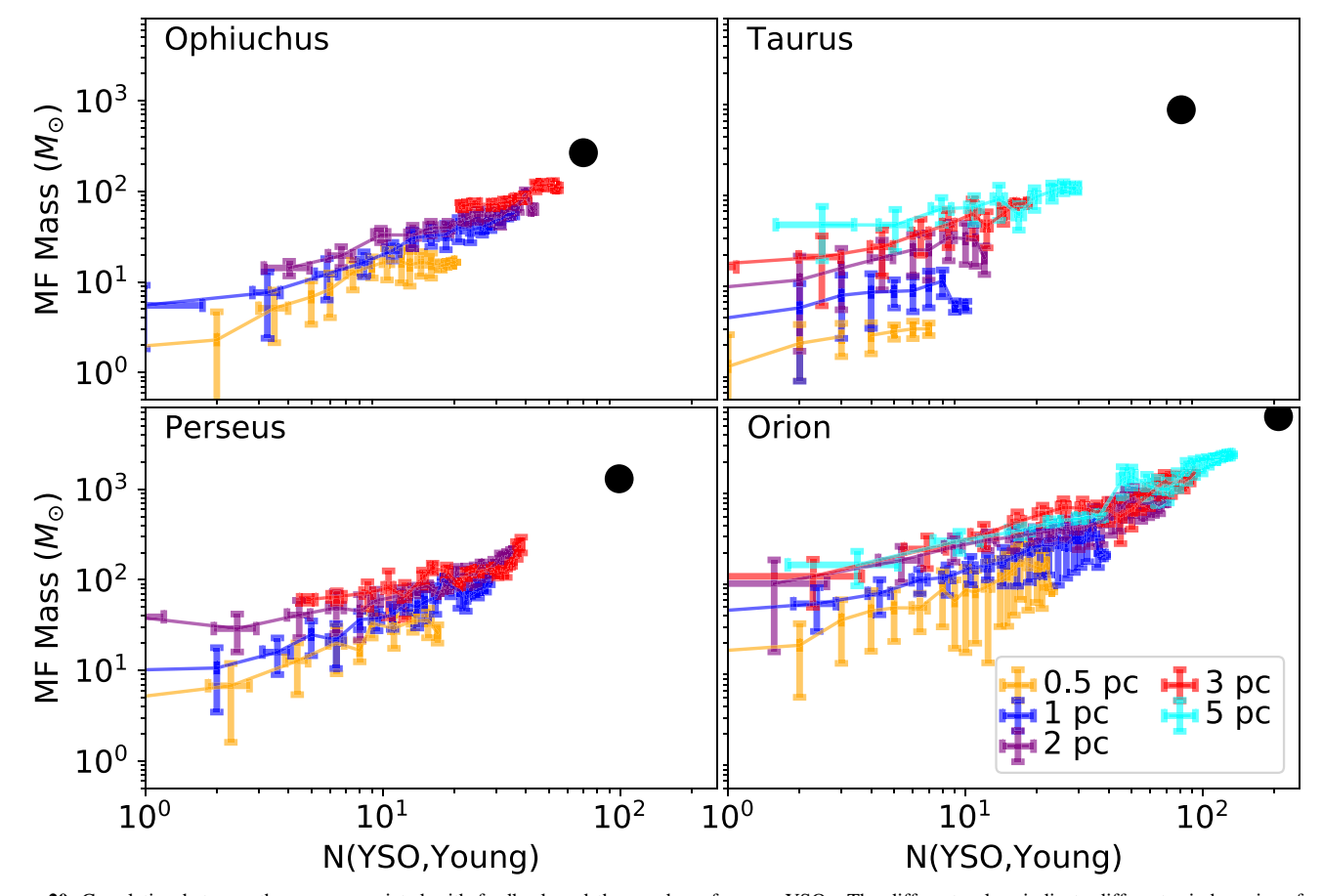


Figure 20. Correlation between the mass associated with feedback and the number of young YSOs. The different colors indicate different window sizes for the estimation. The filled circles indicate the total outflow mass and the total number of young YSOs in the four clouds.

become similar, which indicates the choice of window size does not significantly change the results. Taurus is more sensitive to the window size than the other regions. This is likely caused by the large separations between YSOs. However, it still shows a clear trend of smaller separation between different correlations when the window size gets larger.

The trends are similar when considering total YSOs. Consequently, we conclude that the study of the correlation between the outflow properties and the number of YSOs is robust.

Appendix B Spectra of Outflows and Bubbles

In this section, we employ an unsupervised learning algorithm t-SNE (t-distributed Stochastic Neighbor Embedding) to compare the spectra identified as outflow feedback to those identified as belonging to bubbles. t-SNE is a tool to visualize high-dimensional data by converting the similarities between data points into a low-dimensional manifold. It has been used for classification and outlier detection in a variety of astronomy data (Jofré et al. 2017; Reis et al. 2018; Fluke & Jacobs 2020; Lochner & Bassett 2020). For example, Reis et al. (2018) successfully applied t-SNE to cluster stars based on their spectra and identify outliers based on the t-SNE map.

We take the L1688 star cluster region in Ophiuchus as an example. Figures 3 and 19 show the prediction of this star cluster region by models trained to identify only outflows and only bubbles, respectively. In some cases, the models clearly identify only one or the other type of feedback; however, there is also significant overlap. In order to classify the spectra, we calculate outflow mass and bubble mass of each spectra. If the outflow mass or bubble mass for a given line of sight is above 5σ compared with the background noise, we consider that spectrum to contain feedback. If the outflow mass is larger than the bubble mass, we label it an outflow spectrum. If the bubble mass is larger than the outflow mass, we label it a bubble spectrum. If there is emission but neither outflow mass nor bubble mass exceeds the 5σ threshold, or the spectrum has less than three channels that contain feedback, we label this

spectrum as non-feedback. We neglect any spectra that have no emission above 3σ .

We use the spectra of the L1688 region at each line of sight as input to t-SNE. t-SNE projects the higher-dimensional data into a lower-dimensional (2D) space and organizes it based on similarities (e.g., the line shape and intensity of a spectrum) in the high-dimensional space. Figure 21 shows the t-SNE clusters. We color the data points based on the CASI-3D predictions, where spectra predicted to be primarily associated with outflows are in red, those primarily associated with bubbles are in blue, and non-feedback in black. It is clear that the spectral shapes for bubbles and outflows are different. The spectra of bubbles show two Gaussian components with two peaks of different intensities. The spectra of outflows have various shapes, e.g., broader line wings, and two Gaussian components but with almost equal peaks. It's worth noting that broad line wings are often used to visually identify outflows (Li et al. 2015; Tanabe et al. 2019). t-SNE separates some bubble spectra from the outflow spectra. Meanwhile, we notice that there are some blended/transiting regions, where outflow spectra and bubble spectra are clustered together. In these cases, we find that bubble and outflow identifications have similar spectral shapes. This demonstrates that we cannot distinguish outflows and bubbles based only on single spectra. There is also a mixed region where non-feedback spectra are blended with outflow spectra. The spectral shape of this region indeed shows fewer outflow features, where there is a faint broad line-wing on the blueshifted side.

This analysis explores the similarity between outflow and bubble feedback using an unsupervised machine-learning approach. In some cases, the CASI-3D predictions are clearly distinct. In other cases, where both models identify feedback emission, it is clear that the spectra are truly similar. This may be because both types of feedback can produce such velocity features or because such regions genuinely contain both types of feedback. In the current analysis, it is not possible to distinguish between these two possibilities. However, this t-SNE clustering gives confidence that feedback is shaping these spectra and that CASI-3D is correctly identifying feedback signatures.

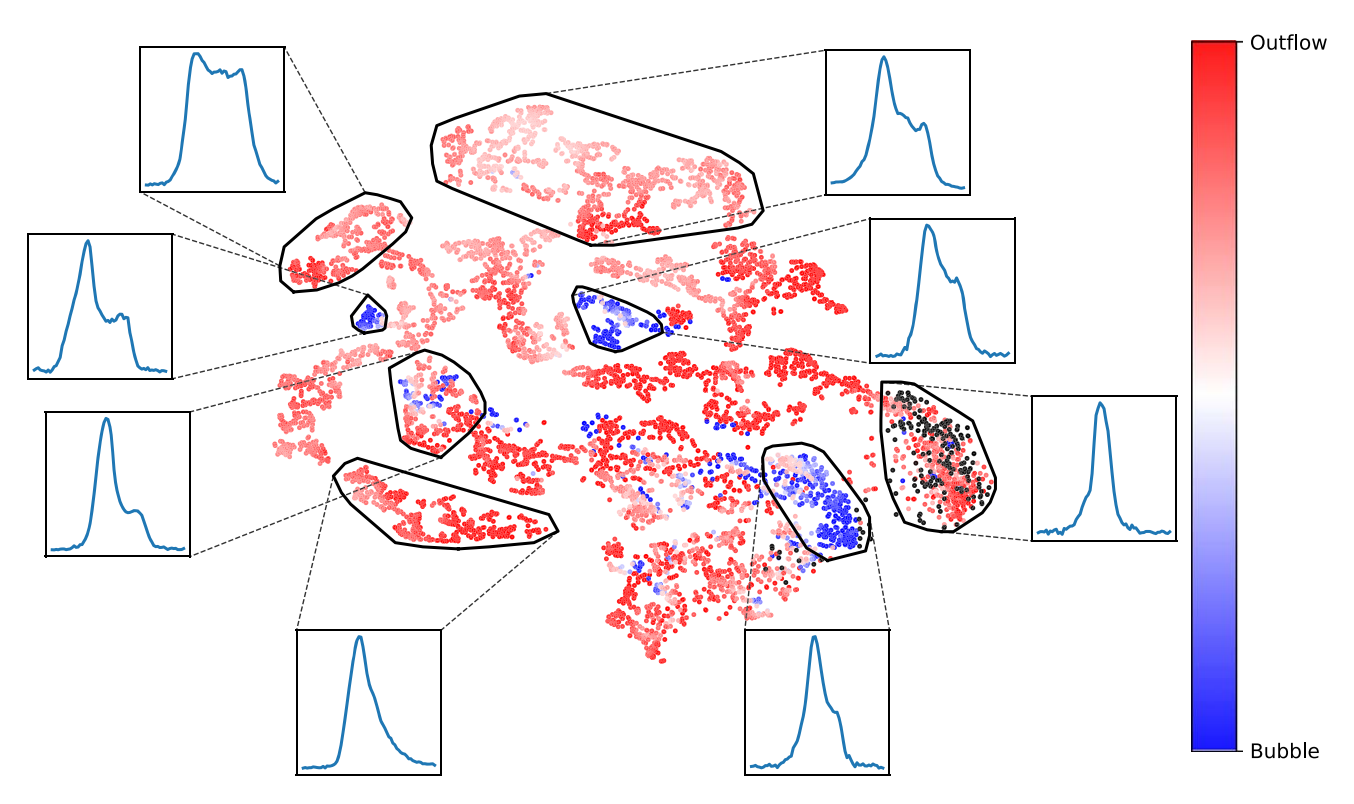


Figure 21. t-SNE map of the ¹²CO spectra in the L1688 star cluster region in Ophiuchus. Red dots indicate outflow spectra. Blue dots indicate bubble spectra. Black dots indicate non-feedback spectra. The sub-plots show the average spectra of each subregion.

Appendix C YSOs in Orion

Orion has an extensive population of older YSOs, so in Figure 8 we plot only the young YSOs for readability. Here, Figure 22 shows the location of both young and old YSOs in

Orion. While we expect younger YSOs to contribute more feedback per source, the large number of older YSOs indicates that they likely contribute feedback throughout the cloud, and this is consistent with the prediction in Section 3.1.4.

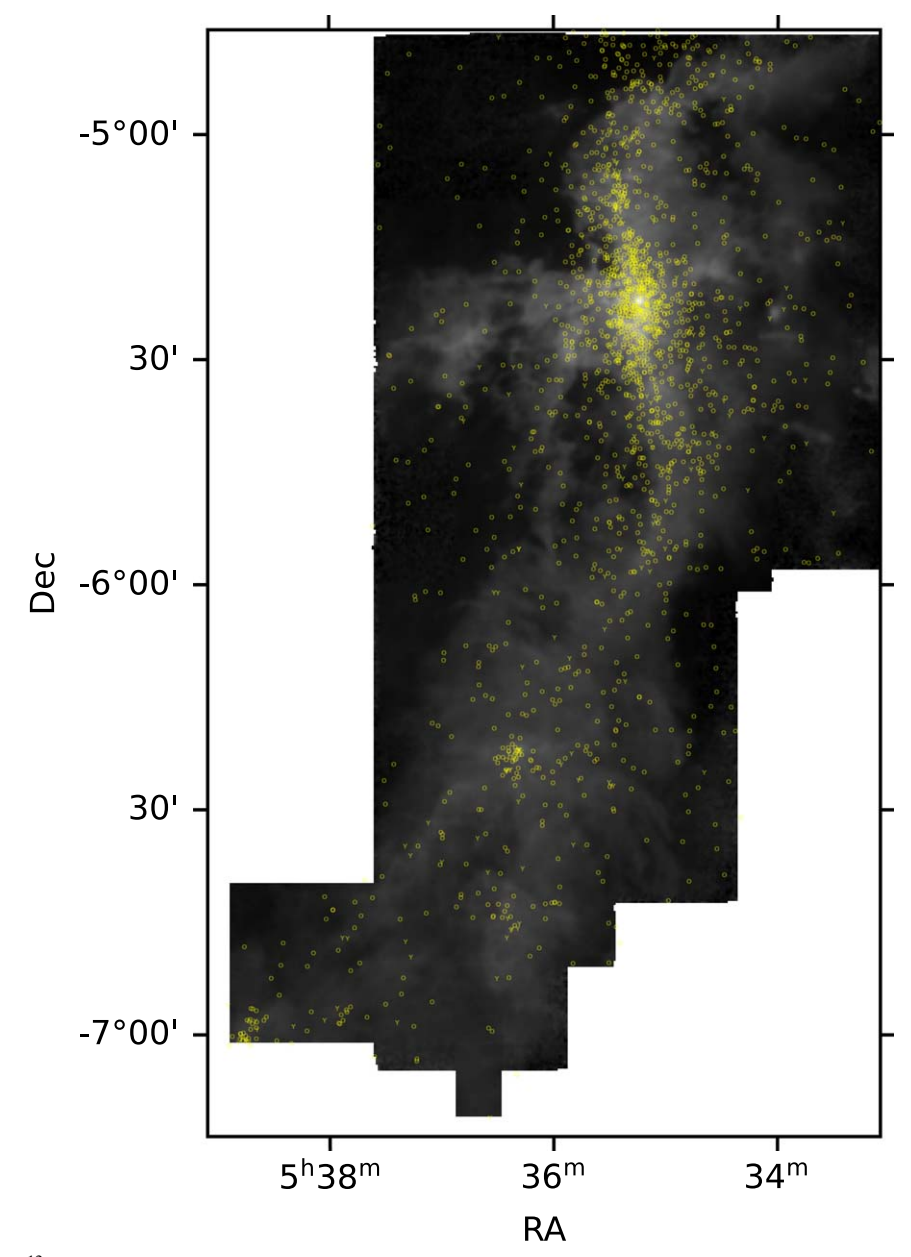


Figure 22. Intensity of ¹²CO integrated over all velocity channels for Orion. Letters "Y" and "O" mark YSO positions, as described in Section 2.3.

Appendix D Outflows in ¹³CO

In some regions, ¹²CO is optically thick, and we combine both ¹²CO and ¹³CO to derive the kinematic estimates rather than using ¹²CO only (e.g., Arce et al. 2010). In most cases, the velocity channels where there is ¹³CO emission dominate the mass in each

spectrum. Here we compare the identification from the ¹²CO map to the ¹³CO emission. Figure 23 shows the ¹³CO emission of the outflow in Figure 9. We can clearly see that the velocity range of ¹³CO is substantially smaller than that of ¹²CO. However, the mass in the ¹³CO emitting region dominates the total mass of the cloud. This also explains why the mass-weighted LOS velocity is smaller than the velocity calculated based on ¹²CO only.

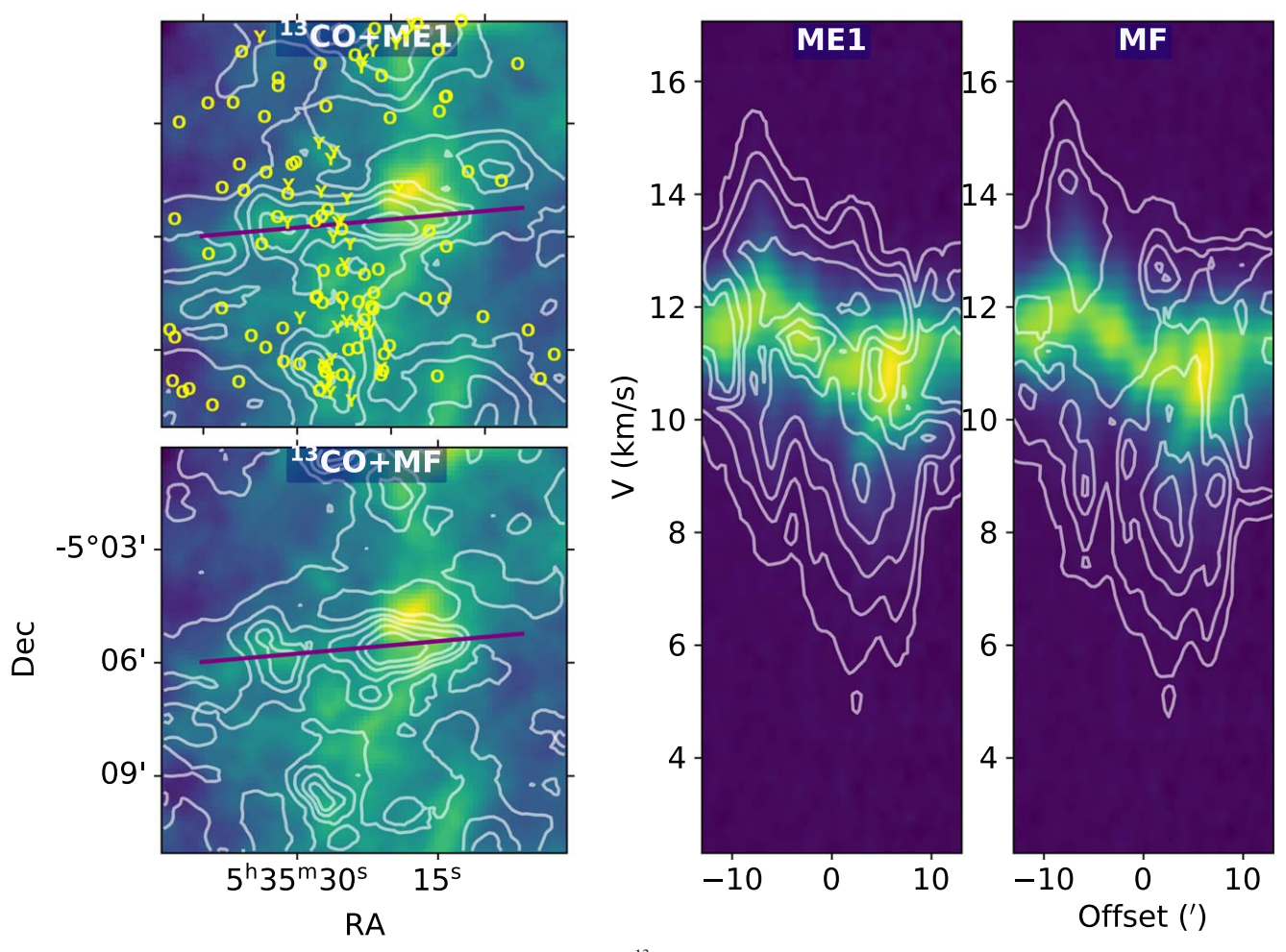


Figure 23. Same as Figure 9 but where the background color-scale indicates the ¹³CO integrated intensity. White contours show the prediction by models ME1 and MF on the ¹²CO data.

Appendix E Correlation between the Gas Mass and the Number of YSOs

In this Appendix, we examine the relationship between the number of YSOs, the total gas mass, and the dense gas mass. Prior work has shown that the number of YSOs is well correlated with the gas column density, which is $\Sigma_* \propto \Sigma_{\rm gas}^2$, or $M_{\rm gas} \propto N_*^{0.5}$ (e.g., Gutermuth et al. 2011; Pokhrel et al. 2020, 2021), where the gas mass was estimated from dust emission. Pokhrel et al. (2020, 2021) found that the surface density of protostars (i.e., younger YSOs) is tightly correlated with gas column following the relation above. Gutermuth et al. (2011) found a similar but less tight relation when considering all YSOs. Consequently, we expect YSOs and dense gas to be correlated. Figure 24 shows a nearly linear relation between the total mass and the number of all YSOs. We find the slope is 0.93, which is slightly smaller than the slope of the outflow mass–YSO relation, 1.03.

To check whether the outflow mass estimate is correlated with the dense gas due to contamination, we examine the relation excluding the rest-frame velocity gas, which is located within the turbulent velocity range ($\pm 1 \text{ km s}^{-1}$). Figure 25 shows the correlation between the total highvelocity gas $(|v - v_{cen}| > 1 \text{ km s}^{-1})$ mass and the number of all YSOs, and the correlation between the high-velocity outflow mass $(|v - v_{cen}| > 1 \text{ km s}^{-1})$ and the number of all YSOs. The slopes are similar to that of the total gas-outflow gas relation including the rest-frame velocity gas. Therefore, we conclude the correlation between gas mass and YSOs exists because outflows are linearly proportional to the number of YSOs launching them. YSOs form from dense gas and thus by nature are more likely to be located in denser regions. By focusing only on the high-velocity material, which traces the outflows most directly, we show that the trend arises directly from the expected correlation between YSOs and outflows rather than indirectly from contamination by the dense gas. This result provides further evidence that our method performs well in dense regions where contamination from the cloud would otherwise be a serious problem.

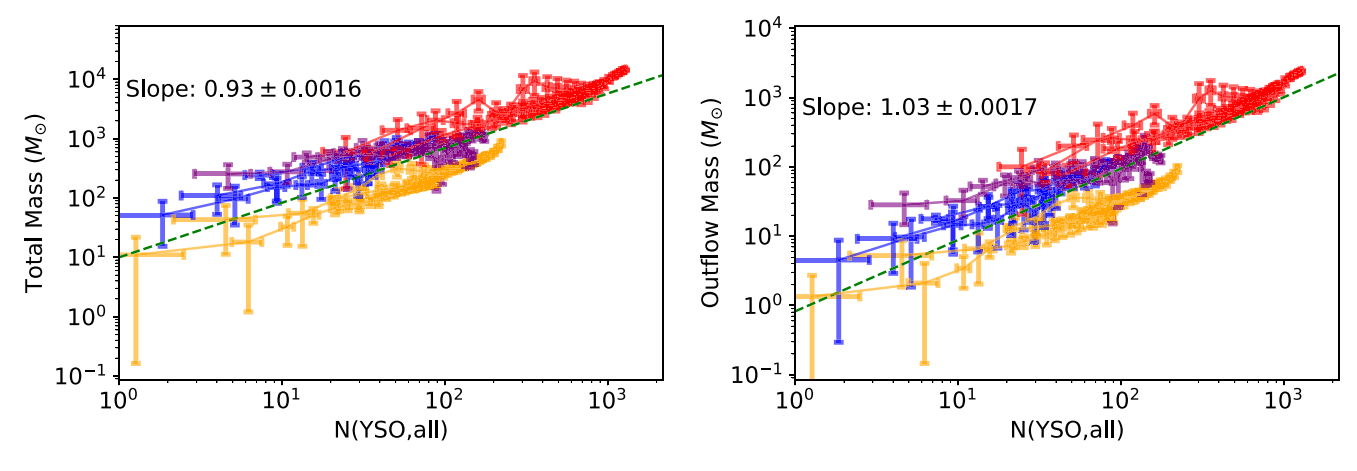


Figure 24. Left: correlation between the total mass and the number of all YSOs. Right: correlation between the outflow mass and the number of all YSOs.

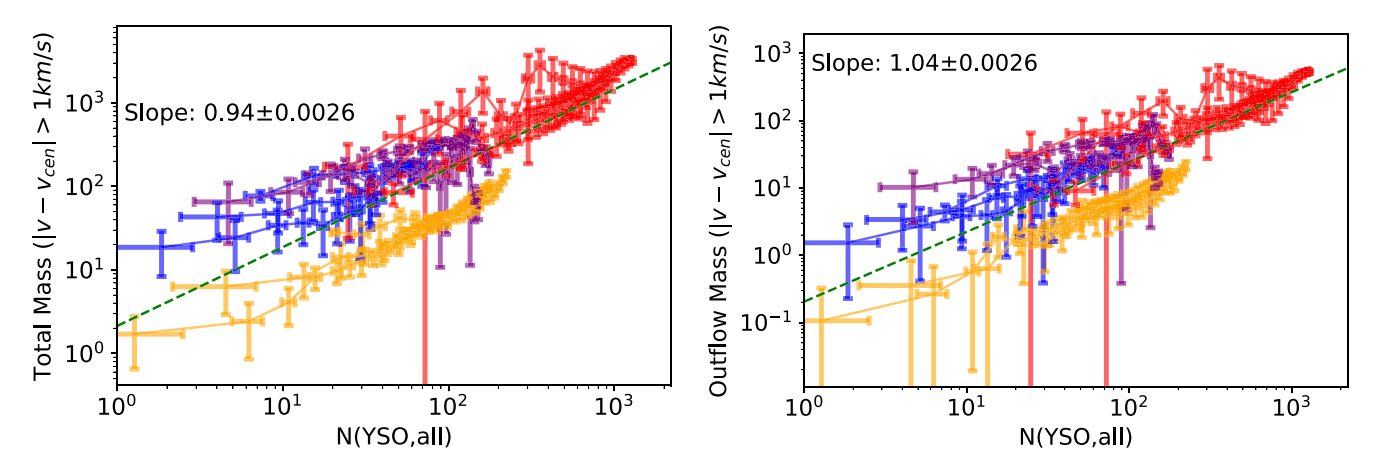


Figure 25. Left: correlation between the total high-velocity gas ($|v - v_{cen}| > 1 \text{ km s}^{-1}$) mass and the number of all YSOs. Right: correlation between the high-velocity outflow mass ($|v - v_{cen}| > 1 \text{ km s}^{-1}$) and the number of all YSOs.

Appendix F CASI-3D Prediction on a Complex Synthetic Observation

In this Appendix, we examine a prediction by the two CASI-3D models on a synthetic observation of a simulation snapshot with a number of interacting outflows. This synthetic observation and the simulation it is derived from are not included in our previous training or testing, so they constitute a more challenging test of the model performance. This simulation is run using a different initial turbulent seed and with twice the initial gas density as the other simulations in the training set. The mean magnetic field strength is $0.8~\mu G$. The evolutionary time of the snapshot is $0.7~t_{\rm ff}$. There are 13 stars launching outflows in the simulation box, whereas our training set is constructed from snapshots with one to five stars. Consequently, this output provides an independent check on the CASI-3D model performance.

Figure 26 shows the integrated CO emission, tracer fractions, and predictions. We find the CASI-3D model does not actually overpredict the amount of emission in the cloud velocity channels but instead slightly underpredicts the location and mass of the outflows. More quantitatively, the model MF identifies 76% of the outflow emission at high-velocity channels (above 2 km s⁻¹). However, the model MF only identifies 40% outflow emissions near the rest-frame velocity (within 2 km s⁻¹). This implies CASI-3D might underestimate the outflow mass by a factor of two. This is consistent with the model uncertainty discussed in Section 4.4. This analysis gives further confidence that CASI-3D correctly excludes contamination from the ambient gas near the rest-frame velocity, even in relatively clustered and complex regions.

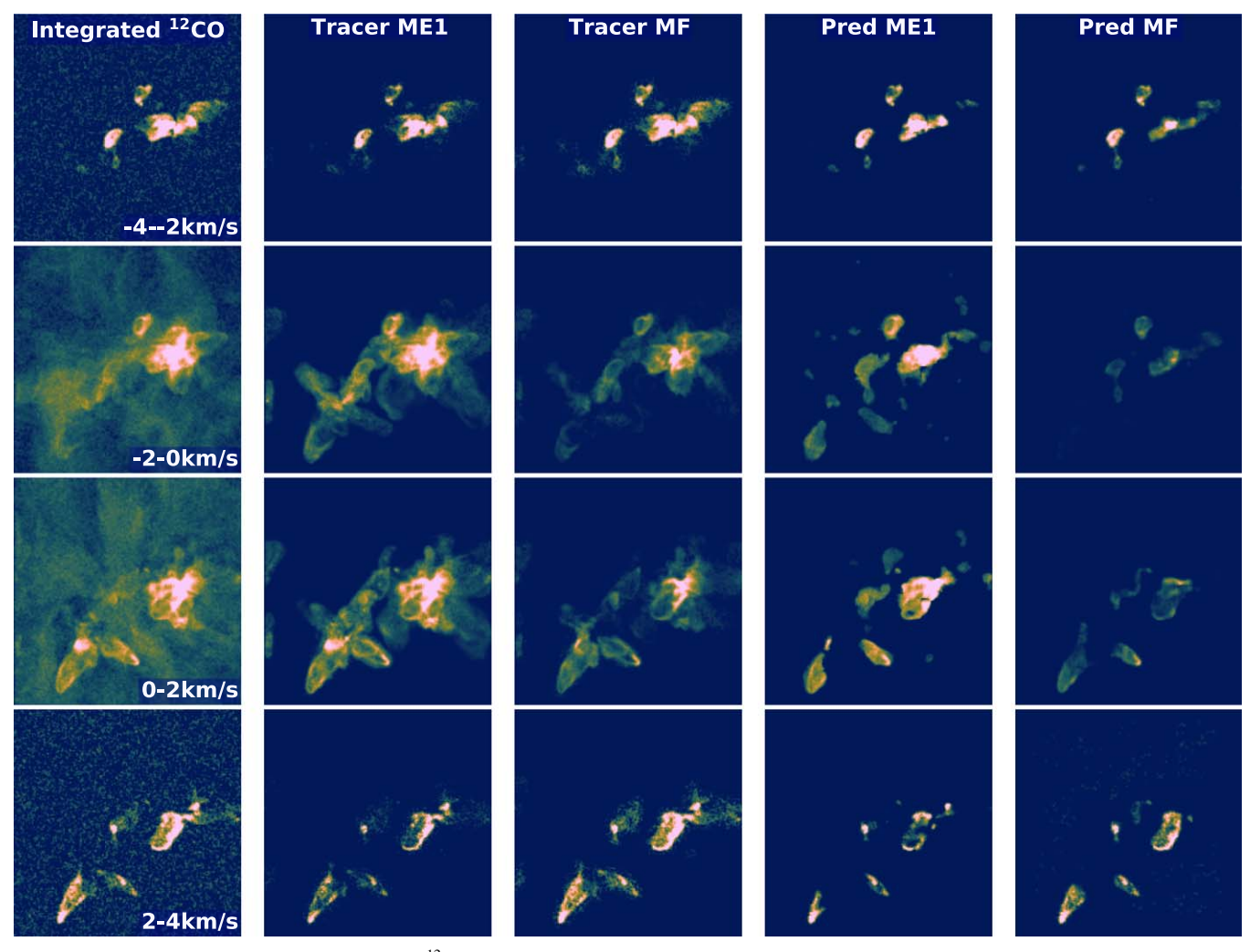


Figure 26. Synthetic ¹²CO observations and CASI-3D prediction in different velocity channels.

ORCID iDs

Duo Xu https://orcid.org/0000-0001-6216-8931
Stella S. R. Offner https://orcid.org/0000-0003-1252-9916
Robert Gutermuth https://orcid.org/0000-0002-6447-899X
Shuo Kong https://orcid.org/0000-0002-8469-2029
Hector G. Arce https://orcid.org/0000-0001-5653-7817

References Arce, H. G., Borkin, M. A., Goodman, A. A., Pineda, J. E., & Beaumont, C. N. 2011, ApJ, 742, 105 Arce, H. G., Borkin, M. A., Goodman, A. A., Pineda, J. E., & Halle, M. W. 2010, ApJ, 715, 1170 Bally, J. 2016, ARA&A, 54, 491 Bontemps, S., Andre, P., Terebey, S., & Cabrit, S. 1996, A&A, 311, 858 Carroll, J. J., Frank, A., Blackman, E. G., Cunningham, A. J., & Quillen, A. C. 2009, ApJ, 695, 1376 Cunningham, A. J., Frank, A., Quillen, A. C., & Blackman, E. G. 2006, ApJ, 653, 416 Cunningham, A. J., Krumholz, M. R., McKee, C. F., & Klein, R. I. 2018, INRAS, 476, 771 Dunham, M. M., Arce, H. G., Mardones, D., et al. 2014a, ApJ, 783, 29 Dunham, M. M., Stutz, A. M., Allen, L. E., et al. 2014b, in Protostars and Planets VI, ed. H. Beuther et al. (Tucson: Univ. Arizona Press), 195 Feddersen, J. R., Arce, H. G., Kong, S., et al. 2020, ApJ, 896, 11 Federrath, C. 2015, MNRAS, 450, 4035 Federrath, C., Schrön, M., Banerjee, R., & Klessen, R. S. 2014, ApJ, 790, 128 Fluke, C. J., & Jacobs, C. 2020, WDMKD, 10, e1349

Frank, A., Ray, T. P., Cabrit, S., et al. 2014, in Protostars and Planets VI, ed. H. Beuther et al. (Tucson: Univ. Arizona Press), 451 Furlan, E., Fischer, W. J., Ali, B., et al. 2016, ApJS, 224, 5 Guszejnov, D., Grudić, M. Y., Hopkins, P. F., Offner, S. S. R., & Faucher-Giguère, C.-A. 2021, MNRAS, 502, 3646 Gutermuth, R. A., Megeath, S. T., Myers, P. C., et al. 2009, ApJS, 184, 18 Gutermuth, R. A., Pipher, J. L., Megeath, S. T., et al. 2011, ApJ, 739, 84 Hansen, C. E., Klein, R. I., McKee, C. F., & Fisher, R. T. 2012, ApJ, 747, 22 He, K., Zhang, X., Ren, S., & Sun, J. 2016, in Proc. IEEE Conf. on Computer Vision and Pattern Recognition (Piscataway, NJ: IEEE), 770 Heitsch, F., Slyz, A. D., Devriendt, J. E. G., Hartmann, L. W., & Burkert, A. 2006, ApJ, 648, 1052 Heyer, M., Goldsmith, P. F., Yıldız, U. A., et al. 2016, MNRAS, 461, 3918 Heyer, M. H., & Brunt, C. M. 2012, MNRAS, 420, 1562 Ishii, S., Nakamura, F., Shimajiri, Y., et al. 2019, PASJ, 71, S9 Jofré, P., Traven, G., Hawkins, K., et al. 2017, MNRAS, 472, 2517 Kirk, H., Friesen, R. K., Pineda, J. E., et al. 2017, ApJ, 846, 144 Klessen, R. S., & Hennebelle, P. 2010, A&A, 520, A17 Kong, S., Arce, H. G., Feddersen, J. R., et al. 2018, ApJS, 236, 25 Li, H., Li, D., Qian, L., et al. 2015, ApJS, 219, 20 Li, Z.-Y., & Nakamura, F. 2006, ApJL, 640, L187 Lochner, M., & Bassett, B. A. 2020, A&C, 36, 100481 Machida, M. N., & Hosokawa, T. 2013, MNRAS, 431, 1719 Matzner, C. D. 2007, ApJ, 659, 1394 Megeath, S. T., Gutermuth, R., Muzerolle, J., et al. 2012, AJ, 144, 192 Moraghan, A., Kim, J., & Yoon, S. J. 2013, MNRAS, 432, L80 Motte, F., Nguyên Luong, Q., Schneider, N., et al. 2014, A&A, 571, A32 Nakamura, F., & Li, Z.-Y. 2007, ApJ, 662, 395 Nakamura, F., Ishii, S., Dobashi, K., et al. 2019, PASJ, 71, S3 Nakamura, F., Kamada, Y., Kamazaki, T., et al. 2011, ApJ, 726, 46 Nakamura, F., Sugitani, K., Tanaka, T., et al. 2014, ApJL, 791, L23

```
Narayanan, G., Heyer, M. H., Brunt, C., et al. 2008, ApJS, 177, 341
Narayanan, G., Snell, R., & Bemis, A. 2012, MNRAS, 425, 2641
Offner, S. S. R., & Arce, H. G. 2014, ApJ, 784, 61
Offner, S. S. R., & Chaban, J. 2017, ApJ, 847, 104
Offner, S. S. R., Robitaille, T. P., Hansen, C. E., McKee, C. F., & Klein, R. I.
   2012, ApJ, 753, 98
Panopoulou, G. V., Tassis, K., Goldsmith, P. F., & Heyer, M. H. 2014,
    INRAS, 444, 2507
Pelletier, G., & Pudritz, R. E. 1992, ApJ, 394, 117
Pokhrel, R., Gutermuth, R. A., Betti, S. K., et al. 2020, ApJ, 896, 60
Pokhrel, R., Gutermuth, R. A., Krumholz, M. R., et al. 2021, ApJL, 912, L19
Rebull, L. M., Padgett, D. L., McCabe, C. E., et al. 2010, ApJS, 186, 259
Reis, I., Poznanski, D., Baron, D., Zasowski, G., & Shahaf, S. 2018, MNRAS,
   476, 2117
Ridge, N. A., Di Francesco, J., Kirk, H., et al. 2006, AJ, 131, 2921
Roccatagliata, V., Franciosini, E., Sacco, G. G., Randich, S., &
   Sicilia-Aguilar, A. 2020, A&A, 638, A85
```

```
Ronneberger, O., Fischer, P., & Brox, T. 2015, in Int. Conf. on Medical Image Computing and Computer-Assisted Intervention (Cham: Springer), 234 Shallue, C. J., & Vanderburg, A. 2018, AJ, 155, 94 Shimajiri, Y., Kitamura, Y., Nakamura, F., et al. 2015a, ApJS, 217, 7 Shimajiri, Y., Sakai, T., Kitamura, Y., et al. 2015b, ApJS, 221, 31 Shu, F., Najita, J., Ostriker, E., et al. 1994, ApJ, 429, 781 Shu, F. H., Lizano, S., Ruden, S. P., & Najita, J. 1988, ApJL, 328, L19 Tanabe, Y., Nakamura, F., Tsukagoshi, T., et al. 2019, PASJ, 71, S8 Van Oort, C. M., Xu, D., Offner, S. S. R., & Gutermuth, R. A. 2019, ApJ, 880, 83
Wang, P., Li, Z.-Y., Abel, T., & Nakamura, F. 2010, ApJ, 709, 27
Wolfire, M. G., Hollenbach, D., McKee, C. F., Tielens, A. G. G. M., & Bakes, E. L. O. 1995, ApJ, 443, 152
Xu, D., Offner, S. S. R., Gutermuth, R., & Van Oort, C. 2020a, ApJ, 890, 64
Xu, D., Offner, S. S. R., Gutermuth, R., & Van Oort, C. 2020b, ApJ, 905, 172
```